

AEDC-TR-73-96

copy 1

ARCHIVE COPY
DO NOT LOAN



ELECTRON BEAM FLUORESCENCE DIAGNOSTICS OF A TERNARY GAS MIXTURE

J. W. L. Lewis and W. D. Williams

ARO, Inc.

July 1973

Property of U. S. Air Force
ARO LIBRARY
F40600-74-C-0001

Approved for public release; distribution unlimited.

VON KÁRMÁN GAS DYNAMICS FACILITY
ARNOLD ENGINEERING DEVELOPMENT CENTER
AIR FORCE SYSTEMS COMMAND
ARNOLD AIR FORCE STATION, TENNESSEE



Property of U. S. Air Force
AEDC LIBRARY
F40600-74-C-0001

NOTICES

When U. S. Government drawings specifications, or other data are used for any purpose other than a definitely related Government procurement operation, the Government thereby incurs no responsibility nor any obligation whatsoever, and the fact that the Government may have formulated, furnished, or in any way supplied the said drawings, specifications, or other data, is not to be regarded by implication or otherwise, or in any manner licensing the holder or any other person or corporation, or conveying any rights or permission to manufacture, use, or sell any patented invention that may in any way be related thereto.

Qualified users may obtain copies of this report from the Defense Documentation Center.

References to named commercial products in this report are not to be considered in any sense as an endorsement of the product by the United States Air Force or the Government.

ELECTRON BEAM FLUORESCENCE DIAGNOSTICS
OF A TERNARY GAS MIXTURE

J. W. L. Lewis and W. D. Williams
ARO, Inc.

Approved for public release; distribution unlimited.

FOREWORD

The work reported herein was conducted by the Arnold Engineering Development Center (AEDC) under sponsorship of the Air Force Rocket Propulsion Laboratory (AFRPL) under Program Element 62301F. The project officer was Captain Jerry Fields.

The results of the research were obtained by ARO, Inc. (a subsidiary of Sverdrup & Parcel and Associates, Inc.) contract operator of AEDC, Air Force Systems Command (AFSC). The work was conducted under ARO Project Nos. VW5216, VW5220, and VY0100 from September 15, 1971, to July 1, 1972. The manuscript was submitted for publication on January 3, 1973.

The authors wish to express their appreciation to A. D. Killian for his aid in the operation and maintenance of the experimental apparatus.

This technical report has been reviewed and is approved.

JIMMY W. MULLINS
Lt Colonel, USAF
Chief Air Force Test Director, VKF
Directorate of Test

A. L. COAPMAN
Colonel, USAF
Director of Test

ABSTRACT

The electron beam fluorescence technique was used for performing spatially resolved density measurements of a ternary gas mixture composed of helium, nitrogen, and hydrogen. The flow field studied was produced by a multinozzle array, and total gas density values exceeded 10^{17} molecules/cc within certain regions of the flow. The experimental apparatus, the procedures, and the method of data reduction used are discussed.

CONTENTS

	<u>Page</u>
ABSTRACT	iii
NOMENCLATURE	vi
I. INTRODUCTION	1
II. THEORY	
2.1 Single-Specie Excitation	2
2.2 Multi-Specie Excitation	4
2.3 Radiative Transitions	6
III. EXPERIMENTAL APPARATUS	
3.1 General Description of Electron Beam System	7
3.2 Optics and Electronics	8
3.3 Flow Visualization	9
IV. CALIBRATION PROCEDURES	
4.1 Excitation and Quenching Cross Sections and Cross-Talk Calibrations	10
4.2 In-Situ Calibration	12
V. DATA ACQUISITION AND ANALYSIS	
5.1 Data Acquisition Procedures	13
5.2 Iteration Procedure	14
5.3 Analysis of Test Data	19
5.4 Error Estimates	20
5.5 Rotational Temperature Measurements	21
VI. SUMMARY AND CONCLUSIONS	22
REFERENCES	23

APPENDIXES

I. ILLUSTRATIONS

Figure

1. Nozzle Bank and Profile Locations	27
2. Excitation- Emission Diagram	28
3. Interaction Diagram for Collisional Quenching	29
4. Partial Energy Level Diagram for Helium, Hydrogen, and Nitrogen	30

<u>Figure</u>	<u>Page</u>
5. Schematic of Electron Beam System Installed on TCTR	31
6. Electron Gun Power Supply	32
7. Two-Stage Orifice	33
8. Photograph of Drift Tube, Orifice, Collector Cup, and Pitot Probe in TCTR	34
9. Electron Beam Collector Cup	35
10. Optical Equipment Arrangement around TCTR	36
11. Optical and Electronic System Schematic	37
12. Filter Transmission Curves	38
13. Helium Signals as a Function of Helium Density	39
14. Collisional Quenching Plot for He 3^1P , He 1^1S Collisions .	40
15. Helium Cross-Talk Signal of Nitrogen and Hydrogen Filters	41
16. Variation of Filter Signals with Hydrogen Density	42
17. Variation of Helium Filter Signal with Nitrogen Density .	43
18. In-Situ Helium Calibration	44
19. Helium Filter Signal as a Function of Helium Density	45
20. Ratio of Helium and Hydrogen Outputs versus x	46
21. Ratio of Helium and Hydrogen Filter Outputs versus Helium Density	47
22. Variation of R_{34} with x	48
23. Iteration Flow Chart	49
24. Variation of Second Iteration of z with Helium Density .	50
25. Variation of Second Iteration of x with x	51
26. Variation of Second Iteration of Helium Density with Helium Density	52
27. Variation of Spectrometer Hydrogen Signal with Hydrogen Ratio x	53
28. Variation of Ratio R_{54} with Hydrogen Ratio x	54

<u>Figure</u>	<u>Page</u>
29. Spectrometer Ratio x'' versus x	55
30. Variation of Spectrometer Hydrogen Ratio with Helium Density	56
31. Filter Signals at Profile 3, $\hat{x}/d = 1.0$, Test Condition No. 6c	57
32. Density Distribution for Profile 3, $\hat{x}/d = 0.13$, Test Condition No. 6c	58
33. Density Distribution for Profile 3, $\hat{x}/d = 1.0$, Test Condition No. 6c	59
34. Mixing-Ratio Distribution for Profile 3, $\hat{x}/d = 0.13$ and 1.0, Test Condition No. 6c	60
 II. TABLES	
I. Radiative Systems and Filter Specifications	61
II. Excitation Coefficients and Ratios	62
III. Collisional Quenching Coefficients	63

NOMENCLATURE

\AA	Angstrom (10^{-8} cm)
$C_{s\mu}$	Coefficient for s^{th} filter, μ^{th} gaseous specie as defined by Eq. (6a)
$C'_{s\mu}$	Excitation coefficient for s^{th} filter, μ^{th} specie, including quenching effects
$C[\lambda_\alpha(ij)]$	Wavelength-dependent spectral sensitivity factor as defined by Eq. (1)
d	Nitrogen-helium nozzle throat diameter
E_B	Electron beam energy
I	Electron beam current
$K_{s\mu}$	Excitation parameter defined by Eq. (8)
$k_{XY}(i)$	Quenching-rate constant of i^{th} state of specie X by specie Y

$k_{\mu\mu}^{(s)}$, (i)	Quenching-rate constant of i^{th} state of specie μ by specie μ for radiation observed in s^{th} filter
L	Beam length
N	Number density
$N_2^+(1-)$	First negative electronic system of N_2^+ molecule
$N_2^+(0, 1)$	0 → 1 vibrational band of $N_2^+(1-)$
$n_X^{(i)}$	Number density of i^{th} level of the X th specie
n_μ	Number density of μ^{th} specie
n_μ'	Number density of μ^{th} specie obtained from filter signal
n_μ''	Number density of μ^{th} specie obtained from spectrometer signal
$n_\mu(\vec{r})$	Position-dependent number density of μ^{th} specie
$R_{ss'}$	Ratio of output signals s and s'
\vec{r}_{1i}	i^{th} location of filter data acquisition
\vec{r}_{2j}	j^{th} location of spectrometer data acquisition
$S_X^{(ij)}$	Photon emission rate per unit electron beam length of specie X for the transition between levels i and j
T	Gas temperature
T'	Optics transmission factor
W(s)	s^{th} filter signal divided by electron beam current
$W(5)_{\text{spec}}$	Hydrogen spectrometer signal
x	Ratio of hydrogen to helium number density
$x^{(i)}$	i^{th} iteration of x
x'	Value of x determined using filter signals
x''	Value of x determined using spectrometer signal
Δx	Axial flow stream distance
y	Mixing parameter $x/(1+z)$
Δy	Coordinate defined by Fig. 1
z	Ratio of nitrogen to helium number density
$z^{(i)}$	i^{th} iteration of z
z'	Value of z determined using filter signals

\hat{z}	Coordinate defined by Fig. 1
α	Indicial subscript denoting specie, as are μ and μ'
$\beta_X^{(ij)}$	Branching factor of i to j transition of X th specie
$\Delta\Omega$	Detector solid angle subtended at the source
$\kappa_{\mu\mu'}^{(s)}$	Product $k_{\mu\mu'}^{(s)}(i) \tau_\mu(i)$
$\lambda_X^{(ij)}$	Wavelength of i to j transition of specie X
$\sigma_X^{(gi; E_B)}$	Excitation cross section for g to i transition of specie X for electron beam energy E_B ; for convenience $\sigma_X^{(gi; E_B)}$ is shortened to $\sigma_X^{(gi)}$
$\tau_X^{(i)}$	Lifetime of level i of specie X

SECTION I INTRODUCTION

Electron beam fluorescence diagnostics of gas dynamic expansion flow fields have been demonstrated during the previous decade to be a valuable source of information under low-density flow conditions. Previous applications of the technique have included spatially resolved measurements of gas density of single-specie flow fields, nitrogen rotational and vibrational temperatures in a variety of flow fields, and gas densities of binary monatomic mixtures expanding from a sonic orifice (Refs. 1-3). Recent applications of the technique at AEDC have extended the utilization of the technique to studies of the interactions of two flow fields (Ref. 4), each composed of a single gas specie, and measurements of both gas density and temperature have been performed. However, all of the aforementioned applications share the characteristics of being low-density and either single or binary gas specie expansions. Extension of the technique simultaneously to higher density (i. e., total-density values on the order of 10^{17} molecules/cc) and multiple-specie flow fields results in a substantial increase in complexity of the measurement and interpretation of the data. Such an increase in complexity is, of course, a result of the requirement to consider collision quenching effects and the existence of radiation "cross-talk" through either optical filters or spectrometers. The problems are further complicated if the observed radiation system of one or more of the species is weak relative to the others. In this event, quenching constants, background correction, cross-talk, and both radiative- and collision-induced cascading effects must be accurately measured. Despite the existence of such difficulties, the requirement of spatially resolved density data for certain testing applications justifies the utilization of the electron beam technique. Included in these applications are diagnostics of exhaust plumes, which are typically multi-specie flow fields, and studies of the gas dynamics of multi-specie interacting flows such as are used for continuous chemical laser systems. It is for the latter application that this work was done.

The gas dynamic source of this investigation was an array of nozzles and jets as shown in Fig. 1, Appendix I. The smaller orifices were hydrogen (H_2) gas sources, and the larger orifices, or nozzles, produced supersonic flows of nitrogen (N_2)/helium (He) mixtures, which were used for simulation of gases actually employed in the chemical laser system. A detailed description of the nozzle bank, operating conditions, and simulation parameters is given in Ref. 5. Using the source

parameters listed in Ref. 5, it was estimated that the order of magnitude of the free-stream total number density would be 10^{17} atoms and molecules/cc. For this flow field, it was desired to study the interactions of the gas dynamic expansions of the H₂ orifices and the N₂/He nozzles. Specifically, it was desired to measure the axial and radial spatial profiles of the absolute value of the number density of the individual species, H₂, He, and N₂. It was also desired to obtain, if possible, information concerning the spatial variation of the gas temperature.

The following sections of this report discuss the theoretical and experimental details of the application of the electron beam fluorescence technique to the nonroutine problem at hand and the degree of success attained in the effort.

SECTION II THEORY

2.1 SINGLE-SPECIE EXCITATION

The interaction of a continuous, high-energy electron beam of energy E_B and current I with atoms or molecules in ground state g produces a steady-state number density in excited quantum state i, n_{X(i)}, and a steady-state detected photon emission rate for beam length L for the i-to-j transition, S_{X(ij)}. It is well known that S_{X(ij)} can be written as

$$S_{X(ij)} = \left(\frac{\Delta\Omega}{4\pi}\right) \times \frac{C[\lambda_X(ij)]\beta_{X(ij)}\sigma_{X(gi;E_B)} \times I \times n_X(g) \times L}{1 + k_{XX}(i)\tau_X(i)n_X(g)} \quad (1)$$

where $\beta_{X(ij)}$ is the branching factor of the i-to-j transition, $\tau_X(i)$ is the lifetime of the state i, and $k_{XX}(i)$ is the total quenching-rate constant for state i. It is noted that both i and j are merely two of a manifold of quantum states for the specie X and its ions. C[λ_{X(ij)}] denotes the effect of the wavelength-dependent optics transmission factor and photocathode sensitivity. The factor ΔΩ/4π represents the source solid angle subtended by the detector and is the location-dependent factor of the equation. If radiative cascading effects are present, it is easily shown that the only change required for Eq. (1) is the replacement of σ_{X(gi;E_B)}, henceforth denoted by σ_{X(gi)}, by

$$\sigma_X(gi) \rightarrow \sigma_X(gi) + \sum_i \sigma_X(gt) \beta_X(ti) \quad (2)$$

where i represents the manifold of states for which the energy eigenvalues exceed the energy eigenvalue of state i . The t -to- i branching factor is denoted by $\beta_X(ti)$. Inclusion of effects due to both collisional quenching of the cascading radiation and collisional induced cascading can be shown to require only the replacement of $\sigma_X(gi)$ in Eq. (1) by the expression

$$\sigma_X(gi) \rightarrow \sigma_X(gi) + \sum_i \sigma_X(gt) \left[\frac{\beta_X(ti) + k_{XX}(ti)r_X(ti)n_X(g)}{1 + k_{XX}(ti)r_X(ti)n_X(g)} \right] \quad (3)$$

where $k_{XX}(ti)$ is the partial quenching-rate constant denoting a collisional transfer process whereby specie X in state t undergoes a transition to state i . Only exoergic processes are considered, and the restrictions on the energy eigenvalues remain as defined for Eq. (2).

The inclusion of cascading effects in Eq. (1) shows clearly the desirability of selecting for use as flow-field diagnostics transitions which are substantially free of both collisional and radiative cascading. Unfortunately, only the latter effect, or its absence, can be deduced from existing data, for collisional quenching constants, both total and partial, are rarely known for cascading states. Additionally, one must rely upon extrapolated values of the excitation cross sections to correct for, or estimate, effects caused by radiative cascading, and this is, in general, possible only for allowed excitation processes due to the paucity of data for high-energy excitation cross sections for first-order-forbidden transitions. Consequently, for diagnostics applications it is desirable to select transitions which are the result of allowed excitation processes so that radiative cascading effects must be caused by excitation processes which are at least first-order forbidden. Subsequent radiative cascading transitions from states excited by such forbidden processes are, in general, much weaker in intensity than radiative transitions from allowed excitation processes, and, as a result, the second terms of both the numerator and denominator of the expression in brackets in Eq. (3) are ignored. For this case, one may write Eq. (1) as

$$S_X(ij)/I = \left(\frac{\Delta\Omega}{4\pi} \right) \times \frac{LC'[\lambda_X(ij)]\beta_X(ij)\left[\sigma_X(gi) + \sum_i \sigma_X(gt) \beta_X(ti) \right] n_X(g)}{1 + k_{XX}(ij)r_X(ij)n_X(g)} \quad (4)$$

and it is seen that $S_X(ij)/I$, an experimentally determined quantity, provides a direct measurement of $n_X(g)$, provided $k_{XX}(i) \tau_X(i)$ is known. The multiplicative factor

$$L \times \left(\frac{\Delta\Omega}{4\pi} \right) \times C[\lambda_X(ij)] \beta_X(ij) \left[\sigma_X(gi) + \sum_t \sigma_X(gt) \beta_X(ti) \right]$$

is determined by an in-situ calibration of the test gas.

2.2 MULTI-SPECIE EXCITATION

Extension of the preceding excitation equation for a ternary gas mixture of species X, Y, and Z provides the set of equations

$$S_\alpha(ij)/I = \left(\frac{\Delta\Omega}{4\pi} \right) \times \frac{LC'[\lambda_\alpha(ij)] \beta_\alpha(ij) \left[\sigma_\alpha(gi) + \sum_t \sigma_\alpha(gt) \beta_\alpha(ti) \right] n_\alpha(g)}{\left[1 + \sum_{\mu=1}^3 k_{\alpha\mu}(i) r_\alpha(i) n_\mu(g) \right]}, \alpha = X, Y, Z \quad (5)$$

where the dummy index μ indicates a sum over the species. It is assumed that heavy particle excitation processes are negligible and, as before, that collisional quenching is the result of a binary collision. Additionally, collisional cascading effects are ignored. Equation (5) shows the additional complexity due to mixture-quenching effects; now three quenching-rate constants are required for each radiative specie.

For many applications, as was the case for this test, the use of optical filters for wavelength isolation is necessitated by requirements placed upon the time available for data acquisition. Typical filters in the visible regime possess bandwidths on the order of 10 to 30 Å, and the use of such filters requires that consideration be given to optical cross-talk effects. For the ternary mixture X, Y, and Z, Fig. 2 shows the likely source of such cross-talk, namely, electron beam excitation of radiative systems of all three species with respective radiation wavelengths within the filter bandpass. Specifically, if specie $\alpha = X$ is to be observed using a specified filter for the i-to-j transition of X, Fig. 2 shows transitions of species Y and Z which can contribute to the filter signal if $\lambda_X(ij)$, $\lambda_Y(kl)$, and $\lambda_Z(mn)$ are approximately equal. As a result, the output signal of the filter selected for observation of the i-to-j transition of specie α is the sum of the signals resulting from the three transitions shown in Fig. 2. Additionally, for the model shown in Fig. 2 one must include, in general, quenching effects on the

cross-talk signals since each "impurity cross-talk" transition may suffer collisional quenching.

Figure 3 shows an interaction diagram for the quenching processes associated with the radiating species of Fig. 2. The parenthetical quantities denote energy levels subject only to the restriction that the initial excited level and the final level are unequal. The specie A(g) represents any of the species X, Y, or Z in the ground electronic state. The quenching constant for the process indicated in Fig. 3, $k_{XA}^{(s)}(i)$, is the quenching rate of excited specie X in level i for collision with specie A in the ground electronic state g. Superscript s denotes that the i-to-j radiative transition of specie X is observed by filter s.

Assuming three filters are to be used for density determinations of the three species, H₂, He, and N₂, one can denote the three current-normalized filter output signals by W(s), s = 1, 2, and 3, and designate the gases H₂, He, and N₂ by the subscripts μ = 1, 2, and 3, respectively. One can now write the filter signals as

$$W(s) = \sum_{\mu=1}^3 \left\{ C_{s\mu} n_{\mu} \right/ \left[1 + \sum_{\mu'=1}^3 k_{\mu\mu'}^{(s)} r_{\mu'}(i) n_{\mu'} \right] \right\}, \quad s = 1, 2, 3 \quad (6a)$$

where $n_{\mu}(g)$ is denoted by n_{μ} and $k_{\mu\mu'}^{(s)}(i)$ denotes the quenching-rate constant of the ith state of the μ th specie by specie μ' as observed in filter s. The coefficient $C_{s\mu}$ is seen, by comparison with Eq. (5), to be

$$C_{s\mu} = \frac{L\Delta\Omega}{4\pi} \times C'[\lambda_{\mu}(ij)] \beta_{\mu}(ij) [\sigma_{\mu}(gi) + \sum_i \sigma_{\mu}(gi) \beta_{\mu}(ti)] \quad (6b)$$

and the value of $C'[\lambda_{\mu}(ij)]$ is dependent on s. Therefore, if no collisional quenching processes exist, then

$$W(s) = \sum_{\mu=1}^3 C_{s\mu} n_{\mu}, \quad s = 1, 2, 3 \quad (7)$$

Thus, for this simplified case nine constants are required, $\{C_{s\mu}\}$, s, μ = 1, 2, and 3. Also, for the more general case including quenching effects, 27 additional constants $\{k_{\mu\mu'}^{(s)}\}$, s, μ , μ' = 1, 2, and 3 are required. Fortunately, in practice many can be ignored, or order-of-magnitude estimates can be utilized.

As will be shown in a following section, the set of equations represented by Eq. (6) can be solved by iteration, thereby obtaining the position-dependent values of number density, $n_\mu(\vec{r})$, $i = 1, 2$, and 3 . Consideration of convergence of the iteration process and accuracy and precision of the data will be discussed in the aforementioned section.

It should be noted that use of additional filters to observe two or more radiative systems of a given specie can, in principle, provide a desirable feature of redundancy for the data. If multiple filters are used in this manner, it is in principle possible to employ modified least-squares fitting to the data for determination of the set of number densities from the over-specifying set of filter output signals.

2.3 RADIATIVE TRANSITIONS

As a result of the short lead-time available before application of the technique to the test, which is described in Ref. 6, it was not possible to perform laboratory measurements to determine the optimum radiative transitions and quenching-rate constants required for the ternary mixture. Order-of-magnitude estimates of unknown quenching-rate constants and excitation cross sections were used, as well as previous experience with N_2 and He, to select the radiative transitions listed in Table I (Appendix II) for the density measurements. It is noted in Table I that two transitions for He were selected: $4^1D \rightarrow 2^1P$ at 4922 \AA and $3^1P \rightarrow 2^1S$ at 5016 \AA ; two transitions for H_2 density measurements were selected: H_β at 4861 \AA and $H_2 G \rightarrow B$ at 4634 \AA ; one transition was selected for N_2 density measurements: N_2^+ first negative (0, 1) band, for which, along with the He 5016-A line, an optical filter was in hand. Figure 4 shows a partial energy level diagram for the three species, and the three radiative transitions, He $3^1P \rightarrow 2^1S$, $N_2^+ (1-)$, and H_β , which were used are indicated thereon. A discussion of the quenching-rate constants and excitation cross sections is presented in Section IV.

SECTION III EXPERIMENTAL APPARATUS

3.1 GENERAL DESCRIPTION OF ELECTRON BEAM SYSTEM

The system required for injecting the high-energy electron beam into the test-gas flow consisted of an electron source, a power supply, and a differential pumping system. A schematic drawing of the electron beam system installed on the Thermo-Chemical Test Rig (TCTR) is shown in Fig. 5. The source of electrons was a GE Type 33 television-type electron gun, with an oxide-coated cathode, modified for 50-kv maximum operation. The accelerator grid had an enlarged opening of approximately 0.48-cm diameter, allowing maximum beam current operation. The power supply for the filament consisted of batteries yielding from 6 to 18 v dc. To obtain the required energy of 40 kv, the anode of the gun was grounded, and the cathode was connected directly to the negative output of a 0 to 50 kv, 0 to 5 ma power supply. Both the grid and the preaccelerator bias voltages were supplied by batteries. Figure 6 shows the circuit diagram of the gun power supply.

The electron gun itself was mounted within a leaktight, insulated Lexan® housing which was maintained at 2 atmospheres (atm) of SF₆, as was the canister containing the filament, preaccelerator, and grid voltage batteries, the voltage divider network, and the tygon tube leading the power supply cables from the battery canister to the electron gun housing. This arrangement prevented arcing and corona discharge.

The beam was magnetically focused and deflected to coincide with a two-stage orifice opening into the test section. The first-stage opening into the test section was of 0.076-cm diameter and 1.26-cm length. The second stage was of 0.127-cm diameter and 0.704-cm length and was separated from the first stage by 0.318 cm. A schematic drawing of the two-stage orifice is shown in Fig. 7, and a photograph of the orifice attached to the electron beam drift tube and mounted in the TCTR is shown in Fig. 8. As can be seen in Fig. 8, the end of the drift tube was water-cooled.

The background, or ambient, gas density into which the electron beam was injected typically exceeded $1 \times 10^{17}/\text{cc}^{-1}$. To maintain the pressure within the electron gun at approximately 10^{-5} torr or less, as required for stable and long-life operation, the orifice was differentially pumped. By referring to Figs. 5 and 7, one can see that the

second stage of the orifice was connected by the drift tube (as shown in Fig. 7) and an external pumping line to a 10-cm diffusion pump. A solenoid-operated, 5-cm gate valve was used to isolate this pump from the drift tube when necessary. The first stage of the orifice was connected by the tubing surrounding the drift tube (as shown in Fig. 7) and an external pumping line to a 7.1 liter/sec mechanical pump.

A precise measurement of beam current was critical for an accurate density measurement. The copper collector cup used for this purpose and shown schematically in Fig. 9 was 5.7 cm long and 3.8 cm in diameter. The interior was carbon-coated, and a double-grid structure was located at the cup entrance. The grids were comprised of approximately 0.040-cm mesh made of about 0.003-cm-diam brass wire and separated by 0.318 cm. The entrance diameter of both grids was 0.127 cm. The interior, or first grid, was negatively biased at 25 to 30 volts (see Fig. 9) to prevent secondary electrons ejected from the cup inner wall from leaving the cup. The outer grid and cup were electrically connected and could be positively biased (see Fig. 9). The entire collector cup was water-cooled and mounted on a sliding vacuum feed-through in order to permit adjustment of the vertical position of the cup (see Fig. 8).

3.2 OPTICS AND ELECTRONICS

The optical radiation produced as a result of electron beam excitation was gathered as shown in Fig. 10 by a double-convex glass lens 25.4 cm in focal length and 10.2 cm in diameter and was focused onto the slit of the optical system, which was housed inside a 1.6-m-long aluminum box mounted on a table adjustable in both the horizontal and vertical planes. A complete schematic of the optical system is shown in Fig. 11. The part of the electron beam fluorescence under observation was located 50.8 cm from the collection lens, and the 1:1 image was therefore formed on the entrance slit 50.8 cm from the collection lens. The optical signal incident on the slit was chopped by a PAR® Model 125 chopping wheel at 333 Hz. The slit was aligned with the long dimension (10 mm) perpendicular to the beam and the short dimension (1 mm) parallel to the beam. Light passing through the slit was gathered by a 7.6-cm-diam, 30.5-cm-focal-length plano-convex quartz lens located 30.5 cm from the entrance slit. An iris diaphragm located in front of this lens allowed the f-number of the housed optics system to be matched with the collection lens f-number. An identical quartz lens separated from the first by a narrow air gap focused the gathered light

onto the photocathode of an RCA-7265 photomultiplier (PM) tube located 30.5 cm from the lens. Immediately in front of the photocathode was located a filter wheel assembly capable of holding eight filters. One of the positions was filled with a piece of frosted glass for alignment purposes, and the other seven positions were filled with filters. The spectral characteristics of these filters are shown in Fig. 12. Five filters were used for number density measurements, and two filters were spectrally located with the (0, 1) band of the $N_2^+(1^-)$ system for rotational temperature determination. The filter wheel could be rotated into the desired position by an externally controlled stepping motor.

Power to the PM was supplied by a Fluke 405B power supply, and the output signal of the PM was processed by a PAR HR-8 lock-in amplifier with the reference signal supplied by the chopping wheel assembly. The PM output was fed into a data logging system for recording on paper and "grocery" tape, or was fed into the Y-axis input of an X-Y plotter for obtaining relative number density profiles. The data logging system also recorded the PM voltage, lock-in amplifier scale, beam current, beam voltage, and TCTR parameters.

In order to more accurately measure the electron beam fluorescence of hydrogen, the optical system in the aluminum box was removed near the end of the test and replaced with a 3/4-m Spex® spectrometer. A dove prism was placed in front of the entrance slit to again make the long dimension (20 mm) of the slit perpendicular to the electron beam image. The slits were opened to 200 μm , and the wavelength was set on 4861 Å (the $H\beta$ line). An EMI-6256B PM tube was mounted at the exit slit, and the PM was maintained at 267°K by cold gaseous nitrogen. The PM signal was processed by an Ortec® photon counting system which included an amplifier, discriminator, and dual counter-timer.

3.3 FLOW VISUALIZATION

For flow visualization photographs, a camera was mounted to observe the flow field through a 7.6-cm-diam quartz window directly across from the window through which spectral measurements were obtained. Since the electron beam was stationary and directed downward from the end of the two-stage orifice, the flow visualization camera had to be moved synchronously with the nozzle bank in order to obtain an axial photograph of the flow field. This was accomplished by attaching the camera support rigidly to the Δ (axial) nozzle bank drive

component, and therefore the camera was moved simultaneously with the nozzle bank. Photographs were obtained by making time exposures while traversing a distance which was usually about 5 cm. Required exposures for obtaining quality photographs were accomplished by camera f-stop adjustments and by varying the Δx -component rate of travel. Black-and-white photographs were taken using a rate of travel of 10.6 sec/cm, and color photographs were taken using a slower rate of 32.3 sec/cm.

The camera used was a Super Speed Graphic® with a 135-mm Graflex Optar® f/4.7 lens and a Graphex-Wollensak® shutter assembly.

Sometimes filters were used with data-point photographs to prevent the predominant radiation of some molecular species excited by the electron beam from exposing the film. Corning sharp-cut 3-70 and 3-72 filters and a Corning 7-59 filter were used, and the transmission curves are shown in Fig. 12.

SECTION IV CALIBRATION PROCEDURES

4.1 EXCITATION AND QUENCHING CROSS SECTIONS AND CROSS-TALK CALIBRATIONS

Referring to Eq. (6b) and recalling that the coefficients $\{C_{s\mu}\}$, $s, \mu = 1, 2$, and 3 contain a common factor which is characteristic of the beam length observed and solid angle subtended by the optics at the excitation point, it is seen that the set of coefficients may be written as

$$C_{s\mu} = \frac{\Delta\Omega L}{4\pi} \times T' K_{s\mu}, \quad s, \mu = 1, 2, 3 \quad (8)$$

where $K_{s\mu}$ now contains only dependencies upon wavelength, excitation cross sections, and cascading processes. The multiplicative quantity T' , of course, is the quantity which exhibits variation due to changes in both the PM tube gain and $\Delta\Omega/4\pi$, the geometrical solid angle subtended by the detector; the latter source of variation, that caused by solid-angle changes, is usually the more significant of the two, and optical realignment is routinely required during data acquisition as a result of inadvertent collisions with the optical apparatus. It is now obvious that for the purpose of calibration it is required only to obtain laboratory measurements of the ratios of $\{C_{s\mu}\}$, $s = \mu = 1, 2$, and 3,

using the intensity of one of the more prominent lines for normalization. Consequently, the in-situ calibration is required to provide only the value of $\Delta\Omega$, once again using the radiative transition which was used for normalization of the laboratory data.

It is to be recalled that the subscript $\mu = 1, 2$, and 3 refers to H_2 , He, and N_2 , respectively, and that $W(1)$, $W(2)$, and $W(3)$ refer to the H_2 filter (the H_β line at 4861 \AA), the $5016\text{-}\text{\AA}$ line filter of He, and the $(0,1)$ band of $N_2^+(1-)$ for N_2 , respectively. The signals $W(4)$ and $W(5)$, defined and used in a following section, are omitted merely for brevity. $W(s)_{\text{lab}}$ and $W(s)_{\text{test}}$ designate laboratory and test chamber measurements, respectively. Also, for determining the ratios of the coefficients $C_{s\mu}$, the $5016\text{-}\text{\AA}$ line He filter with He gas, C_{22} , will be used for normalization. Therefore, the set of ratios $\{C_{s\mu}/C_{22}\}$, $s, \mu = 1, 2$, and 3 must be determined. For this purpose, the laboratory apparatus described in Ref. 6 was used to provide pure-gas samples of H_2 , He, and N_2 . The optical filter signals were determined as a function of the density of the individual species, and Fig. 13 shows a typical result for the excitation of He as observed by both He filters. Using Eq. (6a) for a single specie, it may be seen that this equation can be combined with Eq. (9) to give

$$n_\mu/W(s)_{\text{lab}} = [(-4\pi/\Delta\Omega)_{\text{lab}} \times (1/T' \times K_{s\mu})][1 + k_{\mu\mu}^{(s)}(i)r_\mu(i)n_\mu] \quad (9)$$

Therefore, plotting the left-hand side of Eq. (9) versus n_μ yields not only $C_{s\mu} = (\Delta\Omega/4\pi)_{\text{lab}} \cdot T' \cdot K_{s\mu}$ from the intercept, but also $k_{\mu\mu}^{(s)}(i)\tau_\mu(i)$ from the ratio of the slope and the intercept. Figure 14 shows a typical experimental result. Figure 15 shows the variation of filter signals $W(1)$ and $W(3)$ with He density and, of course, demonstrates the existence of H_2 and N_2 filter signals when observing only pure He, an optical cross-talk effect. Figure 16 shows the variation of all three designated filter signals with H_2 density, and Fig. 17 shows the variation of the He filter signal with N_2 density. Using such data and least-squares fitting to the functional form of Eq. (9), the set of ratios $\{C_{s\mu}/C_{22}\}$, $s, \mu = 1, 2$, and 3 was determined and is listed in Table II. It should be noted that the experimental uncertainty of the coefficients $C_{s\mu}$ was less than approximately ± 5 percent in all cases.

The pure-gas quenching rates $k_{XX}^{(i)}\tau_X(i)$ were determined at room temperature in the manner indicated previously. A complete description of the experimental apparatus, precautions, and data reduction is given by Lewis and Williams (Ref. 6) for the study of the

quenching of atomic hydrogen by H₂. Table III lists the quenching rates employed for this study, and those quenching rates which have not been experimentally determined but have been estimated based on either preliminary data or, hopefully, educated guesses, have been denoted.

4.2 IN-SITU CALIBRATION

Using the electron beam apparatus of the TCTR as described in a previous section, measurements were made of the variation of the W(2) signal with He density, and Fig. 18 shows the result. Using the same analysis procedure as described in the previous section, the coefficient C₂₂ (test) was determined. Therefore, using the equality

$$C_{s\mu}^{(test)} / C_{22}^{(test)} = C_{s\mu}^{(lab)} / C_{22}^{(lab)}$$

the set of coefficients {C_{sμ}(test)}, s, μ = 1, 2, and 3 was generated. Table II lists the results for this set of coefficients. Experimental uncertainty of this set of coefficients is of the same order of magnitude as that of the set of coefficients determined in the laboratory measurements. It should be noted that linearity of the photon emission rate S_X(ij) for each specie with electron beam current was verified over the range of densities observed in the laboratory calibration.

It was observed during the in-situ calibration that the nozzle bank position could effectively change the solid angle of the observation optics ($\Delta\Omega$). Investigation showed that the \hat{y} -position of the cooled nozzle bank had little effect on the observation solid angle. However, at small values of \hat{x} , the \hat{z} -position definitely affected the observation solid angle. With the test section of the TCTR containing a few hundred microns Hg of pure helium, the W(2) signal was measured with the nozzle bank clear of the field of view. As the nozzle bank was moved in the \hat{x} -direction step-wise closer to the electron beam, \hat{z} -axis scans were made, and the W(2) signal was recorded. The \hat{y} -position was set at the zero reference. In this manner, correction factors to $\Delta\Omega$ without nozzle bank interference were determined for the \hat{z} -positions of the nozzle bank at various \hat{x} -locations.

SECTION V DATA ACQUISITION AND ANALYSIS

5.1 DATA ACQUISITION PROCEDURES

The location of the pitot probe with respect to the nozzle bank was determined at the beginning of each day of data-taking. The axial location (\hat{x} -location) was determined by using a transit theodolite located outside the TCTR (see Fig. 10) and focused on the pitot probe through the flow-visualization side window. By arranging the line of sight from the theodolite to the end of the pitot probe perpendicular to the \hat{x} -axis, one could move the nozzle bank close to the pitot probe and record the \hat{x} -position of the scanner in order to provide a reference \hat{x} -location. The \hat{x} -position could be located in this manner within about ± 0.1 mm. The vertical and horizontal (\hat{y} - and \hat{z} -) locations were determined by making \hat{y} - and \hat{z} -pitot-pressure profiles near the exit of the nozzle bank, without H_2 , and reference \hat{y} - and \hat{z} -locations were determined by flow symmetry. The accuracy in the reference \hat{y} - and \hat{z} -locations was better than ± 0.08 mm.

The electron beam was then injected into the flow, and the \hat{x} -location of the beam was determined by the \hat{x} -position of the scanner recorded when the top edge of the nozzle bank moved into the beam and decreased the beam current to half value. The nozzle bank was then moved back, and the horizontal cross hair of the theodolite was adjusted to lie along the axis of the pitot probe, whereas the vertical cross hair lay along the electron beam fluorescence. A slight adjustment of the theodolite focus brought the entrance slit of the optics housing (or spectrometer) on the opposite side of the TCTR into focus. The vertical and horizontal positions of the optics housing were then adjusted until the center of the slit was at the intersection of the cross hairs, with the long dimension of the slit parallel to the pitot probe (or horizontal cross hair). By this method, the \hat{y} -position of the observed portion of the electron beam was the same as the pitot probe \hat{y} -position. The horizontal (\hat{z}) location of the observed portion of the electron beam was determined by making relative number density profiles (PM output recorded on an X-Y plotter) near the exit of the nozzle bank, without H_2 , and by locating the \hat{z} -position by symmetry.

After optical alignment was achieved, flow conditions were set, and number density data were taken at the desired positions in the flow field using the data logging system. At each position, the output of the PM

was recorded with each of the seven filters in the filter wheel in front of the photocathode.

For flow visualization data acquisition, the nozzle bank was moved into the electron beam in such a way that the beam struck the top of the nozzle bank. The camera shutter was opened just before the traverse began, thereby photographing the flow as close as possible to the nozzle exit.

5.2 ITERATION PROCEDURE

The data reduction process utilized filters 1, 3, and 4 and the spectrometer H₂ data, designated as signal 5. Filter 2, the 5016-Å He filter, was not used, for reasons to be explained in the following section.

For the unknown specie distributions of the ternary mixture, the appropriate equation for determination of the density is, of course, Eq. (6a), which can be written as

$$W(s) = \sum_{\mu=1}^3 C'_{s\mu} n_{\mu} , \quad s = 1, 3, 4 \quad (10)$$

where

$$C'_{s\mu} = C_{s\mu} / \left[1 + \sum_{\mu=1}^3 k_{\mu\mu}^{(s)}(i) \times r_{\mu}(i) n_{\mu} \right] \quad (11)$$

Defining the quantities x and z to be n₁/n₂ and n₃/n₄, respectively, one can write the set of equations (10) as

$$W(4) = C'_{42} n_2 [1 + (C'_{41}/C'_{42})x + (C'_{43}/C'_{42})z] \quad (12)$$

$$R_{41} = W(4)/W(1) = [C'_{41}x + C'_{42} + C'_{43}z]/[C'_{11}x + C'_{12} + C'_{13}z] \quad (13)$$

and

$$R_{34} = W(3)/W(4) = [C'_{31}x + C'_{32} + C'_{33}z]/[C'_{41}x + C'_{42} + C'_{43}z] \quad (14)$$

The primary advantage to be gained by ratioing filter signals and obtaining density ratios x and z is the minimizing of the effects of quenching of hydrogen and helium cross-talk on the H_2 density determination. After investigation of several approaches for solution of the three nonlinear equations in three unknowns, the following procedure was adopted.

Using the excitation and quenching coefficients listed in Tables II and III, respectively, a computer calculation was performed of filter output signals for the following ranges of number density:

$$10^{13} \leq n_2 \leq 3 \times 10^{17} \text{ atoms/cc}$$

$$0.0 \leq x \leq 20.0$$

$$0.0 \leq z \leq 10.0$$

The results of the calculation provide information regarding the sensitivity of the measurement over the density domain of interest, indicate the effects of cross-talk, and provide aid in selecting the method of solution of the set of equations. Figure 19 shows the calculated variation of $W(4)$ with both helium density and x , the ratio of hydrogen-to-helium density. The variation of $W(4)$ with z , the ratio of nitrogen-to-helium density, was found to be negligible, and $z = 0.10$ was chosen for the calculation of Fig. 19. Figure 20 shows the variation of R_{41} with x , with n_2 as a parameter. The ratio R_{41} was found to be relatively insensitive to an order-of-magnitude variation in z . However, the sensitivity of R_{41} to He density is severe, and, as a result, relatively accurate values of n_2 must be used in the final determination of x from R_{41} . Figure 21 shows the relative constancy of R_{41} versus n_2 for He density less than approximately 10^{16} atoms/cc and for $x < 0.10$. In addition, the ratio R_{34} was found to be relatively insensitive to the magnitude of x for helium density values less than $5 \times 10^{16} \text{ cc}^{-1}$, as Fig. 22 shows.

The method of solution of Eqs. (12) through (14) was selected to be successive iterations, and the results mentioned in the preceding paragraph indicated the general solution to follow the procedure of determination of n_2 , then z , and finally, x . However, because of cross-talk effects, it is necessary to determine whether the N_2 and He signals, $W(3)$ and $W(4)$, respectively, are caused primarily by a large H_2 concentration at the point in the flow field being measured. If all filter signals are caused predominantly by H_2 , then the procedure of solution should begin with $W(1)$ rather than with an attempt to measure n_1 by

using a cross-talk signal $W(4)$. The actual value of x at which H_2 becomes predominant was determined by consideration of the equation

$$W(1) = C'_{11}n_1[1 + (C'_{12}/C'_{11}) \times (1/x) + (C'_{13}/C'_{11}) \times (z/x)] \quad (15)$$

Equation (15) was used to show that, for $z = 0.10$, if $x \geq 15$, the H_2 signal becomes the most important, which defines the value of x at which the procedure of solution was altered. If x as provided by R_{41} is found to be greater than 15, the procedure of solution requires determination of n_1 , followed by determination of x , and finally, z .

Referring to Eqs. (11) and (12), one recalls that the density-dependence of the results is attributable not only to the explicit dependence of Eq. (12) on n_2 , x , and z , but also to the effects of quenching, as Eq. (11) shows. The iterative method by which the quenching corrections to the coefficients $\{C'_{su}\}$ was achieved is shown in Fig. 23 by means of the flow chart detailing the computer-calculated iterative scheme. From Fig. 23, it may be seen that the first iteration proceeds by obtaining an estimate of x from R_{41} , assuming $z = 0.10$, and using the low-density He curve of Fig. 20. With this value of x , z is then calculated, and these values of x and z are used for a determination of n_2 if $x \leq 15$. At this point, quenching corrections are applied to all cross-talk terms and z is again determined, yielding a value of n_3 . The cross-talk terms are again corrected, and x is calculated using R_{41} , giving n_1 . The cross-talk terms, as well as C'_{42} , C'_{11} , and C'_{33} , are corrected for quenching, and the following iterations proceed in like manner. If $x > 15$, Eq. (15) is used to give n_1 ; R_{41} , to give n_2 ; and R_{43} , to give n_3 . The cross-talk terms are adjusted for quenching as just described, following each density determination. The coefficients C'_{11} , C'_{33} , and C'_{42} are adjusted following determination of the triad (n_1 , n_2 , and n_3). Therefore, the procedure may be summarized by stating that the cross-talk coefficients are maintained current in density estimates as the iteration proceeds, and the main filter coefficients, C'_{11} , C'_{42} , and C'_{33} are one step behind in the sense that the i^{th} iteration for density employs the $(i-1)^{\text{th}}$ values of density for quenching adjustments in C'_{11} , C'_{42} , and C'_{33} .

Employing this iteration scheme, the iterated density values are compared with actual density values for which the "theoretical" calculations were performed. Figure 24 shows the dependence on n_2 of the second iteration of z , $z(2)$. It is seen that $z(2)$ is never more than ten percent larger than z for $n_2 \lesssim 5 \times 10^{16}$ atoms/cc and $0.01 \leq x \leq 1.0$.

Consequently, the iteration procedure is considered satisfactory for z , not only because it differs by ten percent or less over the 0 to 1 torr region at room temperature, but also because its difference from the theoretical value is regular and, therefore, capable of graphical correction. Figure 25 shows the variation of $x(2)$, the second iteration of x , with x , assuming $z = 0.10$, for various values of n_2 . It is seen that at the higher values of He density, $x(2)$ deviates significantly from x . Figure 26 shows the second iteration of He density as a function of n_2 for $x = 0.10$ and 10.0, assuming $z = 0.10$.

As described in a previous section, detection of the H_β line of H_2 was also performed using a spectrometer, rather than a broad bandpass filter, and photon-counting electronics. The spectrometer output signal, after being normalized by the electron beam current, can be written as

$$W(5) = \sum_{\mu=1}^3 C'_{5\mu} n_\mu \quad (16)$$

where $C'_{5\mu}$ is defined by Eq. (11). The coefficients C_{51} and C_{52} obtained by an in-situ calibration are listed in Table II. It is seen that the cross-talk effect has been reduced by approximately a factor of four by using spectrometric rather than filter detection. Figure 27 shows the variation of $W(5)$ with x for various values of He density.

One now has filter signals for He and N_2 densities, a spectrometer signal $W(5)$ for H_2 density, and a filter signal $W(1)$ for H_2 density which is of lesser reliability than $W(5)$. Two iteration procedures were employed to obtain values of H_2 density using primarily $W(5)$ and values of He and N_2 density using primarily $W(4)$ and $W(3)$, respectively.

The first procedure of solution is as follows: From Eqs. (11) and (16), it may be seen that the set of density values (n_1 , n_2 , and n_3) is required for both cross-talk and quenching corrections. The values of n_1 , n_2 , and n_3 provided by the filter outputs and denoted by (n'_1 , n'_2 , and n'_3) were used in the cross-talk term $C'_{52} n'_2$, and n'_2 and n'_3 were used in the quenching term of the denominator of C'_{51} . The value of H_2 density n''_1 then obtained from $W(5)$ can be written as

$$n''_1 = g(1 + h) / (C_{51} - g \times \kappa_{11}^{(5)}) \quad (17)$$

where

$$g = W(5) - C'_{52} \times n'_2$$

and

$$h = \kappa_{12}^{(5)} n'_2 + \kappa_{13}^{(5)} n'_3$$

Results of the computational procedure indicated that n'_1 exhibited excessively large sensitivity to the iterated value of He density n'_2 ; therefore, this procedure was discarded in favor of the procedure which is described in the following paragraphs.

The ratio R_{54} of signals $W(5)$ and $W(4)$ was formed and is defined by

$$R_{54} = \frac{\sum_{\mu=1}^3 C'_{5\mu} n_{\mu}}{\sum_{\mu=1}^3 C'_{4\mu} n_{\mu}} \quad (18)$$

and Fig. 28 shows the variation of R_{54} with H_2 ratio parameter, x , for various values of He density. It may be seen from Fig. 28 that the sensitivity of the determination of x using R_{54} decreases with increase in He density, an effect which is attributable to both cross-talk and quenching effects. Defining x'' as the H_2 ratio parameter obtained from Eq. (18) and Fig. 20, it is seen that

$$x'' = [R_{54}(C'_{42} + C'_{43}z) - C'_{52} - C'_{53}z]/[C'_{51} - R_{54}C'_{41}] \quad (19)$$

Using the computer-calculated values of R_{41} , R_{34} , and $W(4)$, the values of number density (n'_1 , n'_2 , and n'_3) were obtained by the previously described iteration process. These values of number density were then employed for the quenching corrections to Eq. (19) and, using the theoretical value of R_{54} , x'' was determined. Figure 29 shows the variation of x'' with the actual value of x for various values of n'_2 . It is seen that the discrepancy between x'' and x is a monotonic function of x so long as $n'_2 \leq 1 \times 10^{17}$ atoms/cc. For larger values of n'_2 , each data point must be considered on an individual basis for determination of x . Figure 30 shows the functional behavior of $x''(2)$ with respect to n'_2 for various values of x , and the correction-free regime of $x(2)$ versus n'_2 is indicated.

5.3 ANALYSIS OF TEST DATA

For the flow field investigated, the description and results of which are presented in Ref. 5, the spatial profiles of the position-dependent specie density $n_\mu(\vec{r})$ were determined using the apparatus and the acquisition and data reduction techniques described in previous sections. As was previously mentioned, both filter and spectrometer data were obtained for the measurement of H_2 density, and a separate test entry was made to obtain the spectrometric data of n_1 . Since the spatial locations at which the filter and spectrometer data were acquired were not exactly coincident, it was necessary to employ a spatial interpolation technique to reduce the spectrometer data. This was required because both the spectral cross-talk and the quenching correction terms are present in the $W(5)$ equation. Therefore, if $\{\vec{r}_{1i}\}$, $i = 1, 2, \dots, N$, represents the N spatial locations within a profile of filter data, as defined by Fig. 1, and $\{\vec{r}_{2j}\}$, $j = 1, 2, \dots, N$, the N spatial locations of spectrometer H_2 data within the same profile, it is seen that the values $n_\mu(\vec{r}_{2j})$ are required to reduce the spectrometer data. However, only $n_1(\vec{r}_{2j})$, $j = 1, 2, \dots, N$, exist. Therefore, it was necessary to interpolate the filter number density data $n_\mu(\vec{r}_{1i})$, $i = 1, 2, \dots, N$, to obtain the values at the positions $\{\vec{r}_{2j}\}$, $j = 1, 2, \dots, N$. For this purpose, the results were selected so that $|\vec{r}_{1i}| < |\vec{r}_{2j}| < |\vec{r}_{1i+1}|$, and, additionally, for all cases $|\vec{r}_{1i+1} - \vec{r}_{1i}| \gg |\vec{r}_{2j} - \vec{r}_{1i}|$, thereby minimizing interpolation error. It was assumed that the values $n_\mu(\vec{r}_{1i})$ and $n_\mu(\vec{r}_{1i+1})$ were accurately connected by a linear relationship to allow prediction of $n_\mu(\vec{r})$ at any position between \vec{r}_{1i} and \vec{r}_{1i+1} . Having accomplished this, one has values of $n_\mu(\vec{r}_{1j})$ which are used in Eq. (19) for a determination of $n_1(\vec{r}_{2j})$, the spectrometer result.

The initial reduction of the data used the 5016-Å He filter in place of the 4922-Å signal. All previously presented equations and figures involving filter 4, the 4922-Å filter, had corresponding equations and figures using filter 2. The iteration procedure used with $W(2)$ rather than $W(4)$ was identical to that just presented. The n_2 results, however, showed an excessively large value of helium density with the obvious discrepancy worsening in regions where the He density would be expected to be largest. Moreover, the experimental values of $W(2)$ in some regions of the flow field were larger than the theoretical maximum value of n_2 which was predicted by Eq. (10) with $s = 2$. Figure 31 shows a typical experimental result of the acquired filter signals $W(1)$, $W(2)$, $W(4)$, and $W(5)$ for Profile 3 at $x/d = 1.0$ for Test Condition 6c, as defined in Ref. 5. The theoretical maximum for $W(2)$ is on the order of 40 output units, and yet $W(2)$ exceeds 100 output units at

$y = -0.5$ cm. The $W(4)$ signal follows quite closely the qualitative behavior of $W(2)$ and is less than its maximum value. This latter observation eliminates the possibility of a beam current avalanche phenomenon as being the source of the discrepancy. The possibility of calibration error is eliminated since the n_2 values derived from $W(2)$ and $W(4)$ agree in the low-density regions of the flow field. A third possible cause of the anomalous behavior is the existence of contaminant radiation, or excessive cross-talk. The He 5016-Å filter calibration data for N_2 and H_2 density variations did not exhibit anomalously large cross-talk effects, but it should be noted that the calibration data were acquired for gas number density values less than 6×10^{16} atoms/cc, which is equivalent to 2 torr at 300°K. Consequently, data acquired when $n_2 \gtrsim 1 \times 10^{17}$ atoms/cc may well show discrepancies not predicted. Likely sources of such cross-talk effects are the atomic nitrogen ion lines at 5045.1, 5025.7, and 5016.4 Å, all within the 5016-Å filter passband. Because of these results, all flow-field data were analyzed using the signal $W(4)$.

Figure 32 shows the results of the density distributions for Profile 3, $\Delta/d = 0.13$, and Fig. 33, $\Delta/d = 1.0$, using the method of data reduction just outlined. These results show the extremely high value of gas density obtained for this flow-field profile, and the regions of H_2 flow are also clearly seen. The complex axial and radial density distributions are presented in Ref. 5. An additional parameter of interest for these studies of a chemical laser nozzle array is the ratio, y , of $n_1(\vec{r})$ and the sum of $n_2(\vec{r})$ and $n_3(\vec{r})$. This ratio, y , is a measure of the gas-mixing and nozzle interaction effects between the flow field composed solely of H_2 and the binary mixture flow field of He and N_2 . It may be seen that

$$y(\vec{r}) = x(\vec{r})/[1 + z(\vec{r})] \quad (20)$$

where the position dependencies of x , y , and z are parenthetically denoted by \vec{r} . The experimental values of $y(\vec{r})$ corresponding to the data of Fig. 24 are shown in Fig. 34.

5.4 ERROR ESTIMATES

The confidence level of these experimental results is a complicated function of the test parameters and specie number density values of the flow field. Consequently, only a qualitative discussion of sources of error is possible.

The precision of the number density data is due both to the repeatability of the spectrometric signals and the sensitivity of the measurement. The filter and spectrometer signals $W(s)$, $s = 1, 2, 3, 4$, and 5, were obtained at least twice at each spatial location, and these data were typically reproducible to within ± 5 -percent deviation from the mean. For the low-density portions of the flow field, this implies a ± 5 -percent imprecision of the resulting density data. However, as Fig. 19 clearly shows, this same value of imprecision yields ever-increasing values of imprecision in the density values as the specie densities increase. Consequently, one must conclude that the density data are imprecise by approximately ± 10 percent over the regime of applicability of the technique.

Values of accuracy to be assigned to the data are more difficult to determine. It is felt that the major source of inaccuracy of the resulting specie density values is a result of both the imprecision of the quenching constants, which is typically ± 15 percent for the most significant rate processes, and the inaccuracy of the quenching constants resulting from a neglect of their temperature dependence. Concerning the temperature dependence of the rate constants, it should be noted that the assumption of hard-sphere binary collision processes yields a \sqrt{T} dependence for the rate constant and indicates that as the expansion proceeds, producing lower gas temperatures and densities, the effects of quenching become less important. However, no evidence to support a hard-sphere hypothesis exists, and for some species, such as N_2^+ , contrary evidence exists. Since the quenching correction at high density values was greater than 100 percent, the overall uncertainty of the results for these regions is perhaps no less than approximately ± 25 percent. For flow-field regions of less than approximately 10^{16} cc^{-1} , total density uncertainty values of approximately $\pm 15\text{-}20$ percent may be realistic. Additionally, it should be noted that values of the mixing ratio y may be of lower uncertainty than the just-quoted values as a result of minimizing quenching corrections by the signal-ratioing procedure.

5.5 ROTATIONAL TEMPERATURE MEASUREMENTS

As is described in Section 3.2, two filters, spectrally located within the $(0, 1)$ band of the $N_2^+(1^-)$ system, were used to obtain data in an attempt to determine the rotational temperature of N_2 . Restrictions placed upon data acquisition time precluded performing measurements of the spectrally resolved rotational structure of the vibrational bands of the $N_2^+(1^-)$ system. The filters used (maximum transmission at

4258 Å and 4278 Å, 8-Å half-width) in principle provided signals which when ratioed yielded the rotational temperature of N₂. These data were acquired for the entire flow field studied. However, calibration of the filter ratio signals required not only measurements of N₂ over wide temperature and density ranges but also calibration for quenching effects due to both He and H₂. Unfortunately, time was not available to complete these calibrations, but the raw experimental data are available for reduction at a later time if interest warrants such an effort.

SECTION VI SUMMARY AND CONCLUSIONS

The results shown in Figs. 31-34 and in Ref. 5 demonstrate the applicability of the electron beam fluorescence technique to diagnostics of a ternary gas mixture of relatively high densities. The preceding discussion and figures clearly indicate the limit of applicability for the flow field investigated. Useful data were obtained at total density values exceeding $1 \times 10^{17} \text{ cc}^{-1}$, corresponding to 3 torr at 300°K. Because of the small physical size of the flow field, beam-spreading was not severe, and the spatial resolution was adequate.

The apparently excessive values of z measured in the flow cores of the N₂/He flow field may possibly be explained for the high-density portions of the field as caused by collisional energy transfer to N₂ from metastable He atoms, resulting in enhanced N₂ radiation. Although gas separation effects can not be eliminated as a possible cause, the metastable excitation source hypothesis appears to be the more probable explanation. The use of additional N₂⁺ radiative transitions for measurement of N₂ density would provide an indication of the validity of this suggestion, since it is believed that resonance excitation transfer processes are a sensitive function of the amount of energy being transferred. Therefore, if indeed it is the He 2¹S state populating the N₂⁺ B² Σ_u⁺ state by a quasi-resonance energy transfer process, then radiative transitions from different vibrational levels of the N₂⁺ B² Σ_u⁺ state may yield systematically different values of N₂ density. This would confirm the hypothesis.

The degree of optical cross-talk of the filters and spectrometers emphasizes the necessity for accurate determinations of electron excitation cross sections of the various gas species typically encountered in such test facilities. This is particularly important for those species

for which the main radiative transition systems are weak relative to those of the other flow constituents. Such was the case of H₂, the radiation from which was the result of a dissociative-excitation process.

REFERENCES

1. Williams, W. D., Hornkohl, J. O., and Lewis, J. W. L. "Electron Beam Probe for a Low Density Hypersonic Wind Tunnel." AEDC-TR-71-61 (AD727004), July 1971.
2. Rothe, D. E. "Electron Beam Studies of the Diffusive Separation of Helium-Argon Mixtures in Free Jets and Shock Waves." UTIAS Report No. 114, July 1966.
3. Lewis, J. W. L. and Williams, W. D. "Vibrational Temperature Measurements Using the Electron Beam." AIAA Journal, Vol. 7, No. 6 (June 1969), 1202-1204.
4. Norman, Wendell, Kinslow, Max, and Lewis, J. W. L. "Experimental Study of Simulated High Altitude Rocket Exhaust Plumes." AEDC-TR-71-25 (AD726555), July 1971.
5. Whitfield, D. L., Lewis, J. W. L., and Williams, W. D. "Species Number Density, Pitot Pressure, and Flow Visualization in the Near Field of Two Supersonic Nozzle Banks Used for Chemical Laser Systems." AEDC-TR-73-11, May 1973.
6. Lewis, J. W. L. and Williams, W. D. "Collisional De-Excitation Cross-Section Measurement of Electronic States of Atomic and Molecular Hydrogen by Collision with Molecular Hydrogen." AEDC-TR-72-132 (AD750464), October 1972.

APPENDIXES

- I. ILLUSTRATIONS**
- II. TABLES**

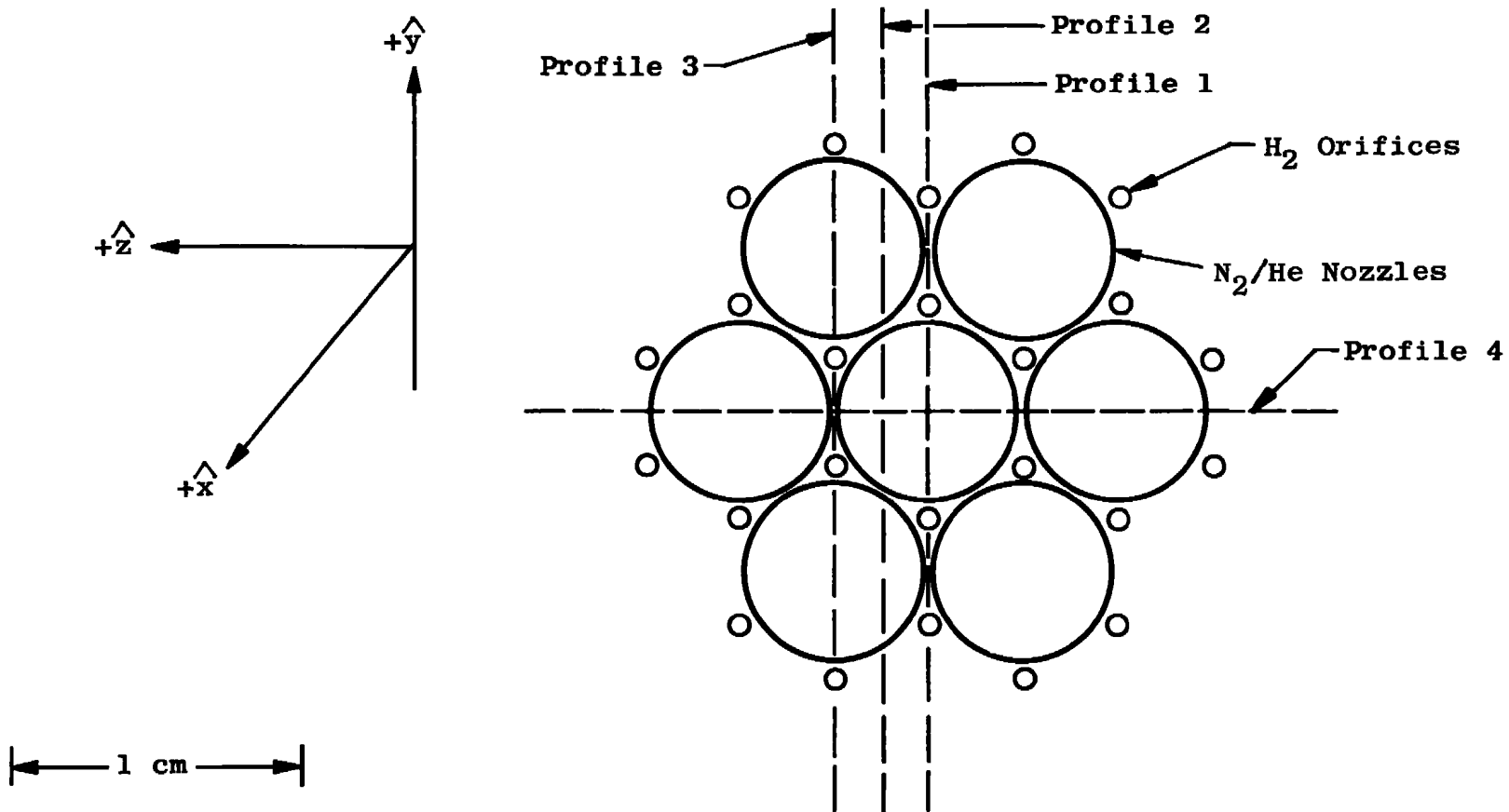


Fig. 1 Nozzle Bank and Profile Locations

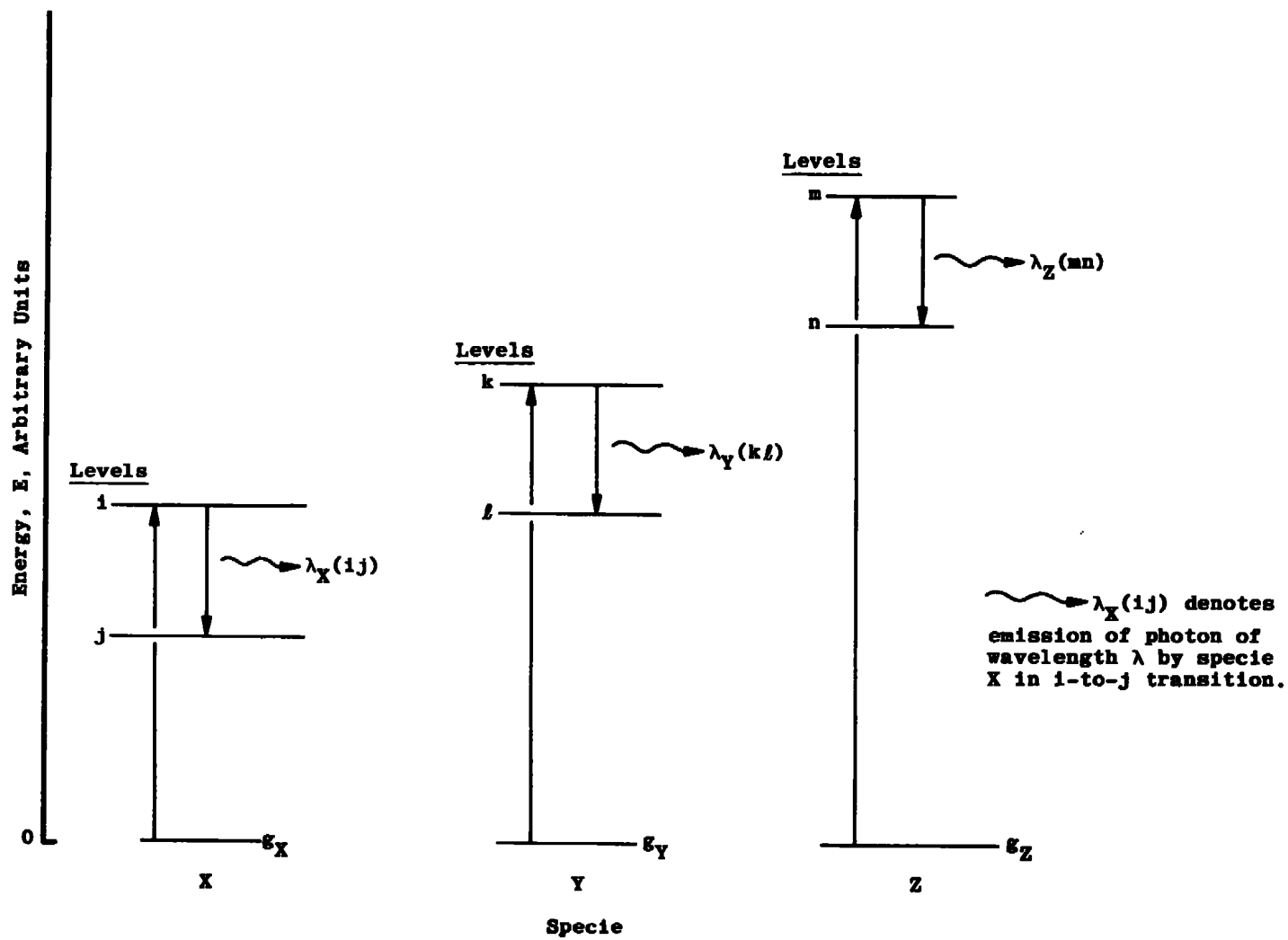


Fig. 2 Excitation-Emission Diagram

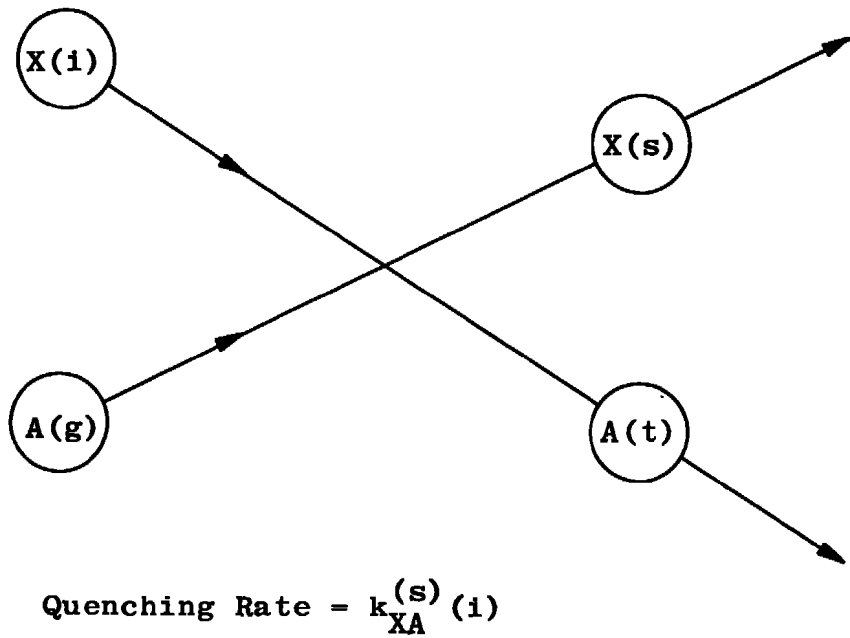


Fig. 3 Interaction Diagram for Collisional Quenching

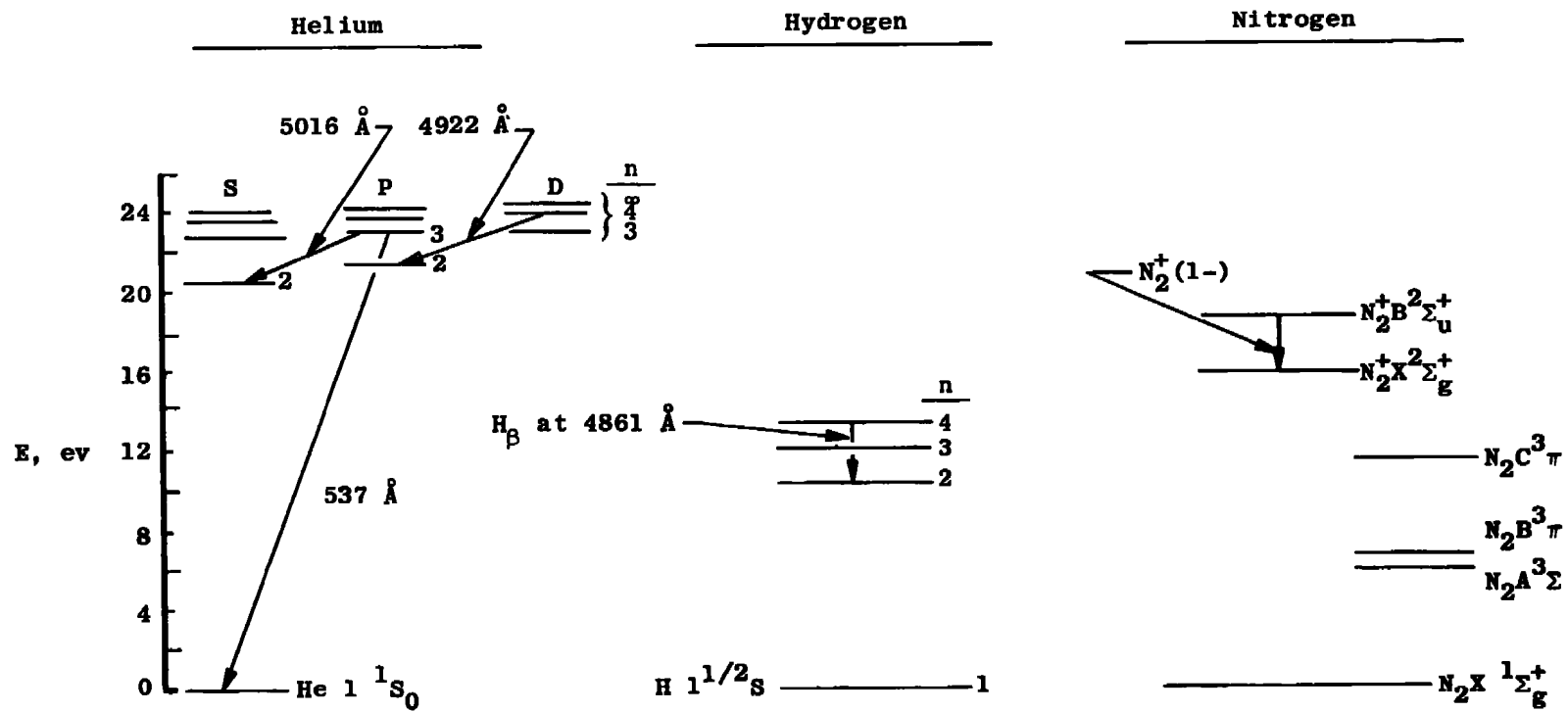


Fig. 4 Partial Energy Level Diagram for Helium, Hydrogen, and Nitrogen

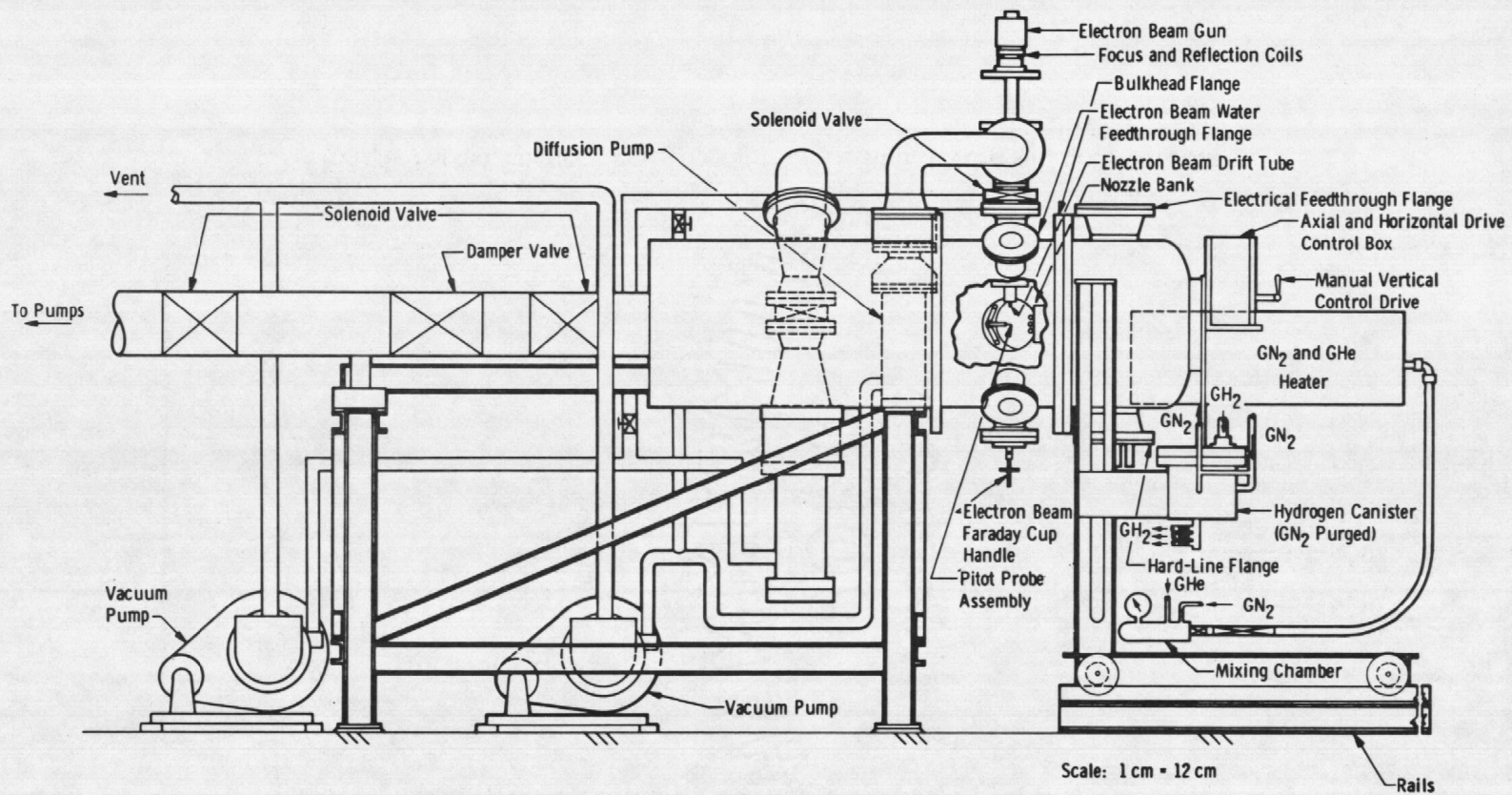


Fig. 5 Schematic of Electron Beam System Installed on TCTR

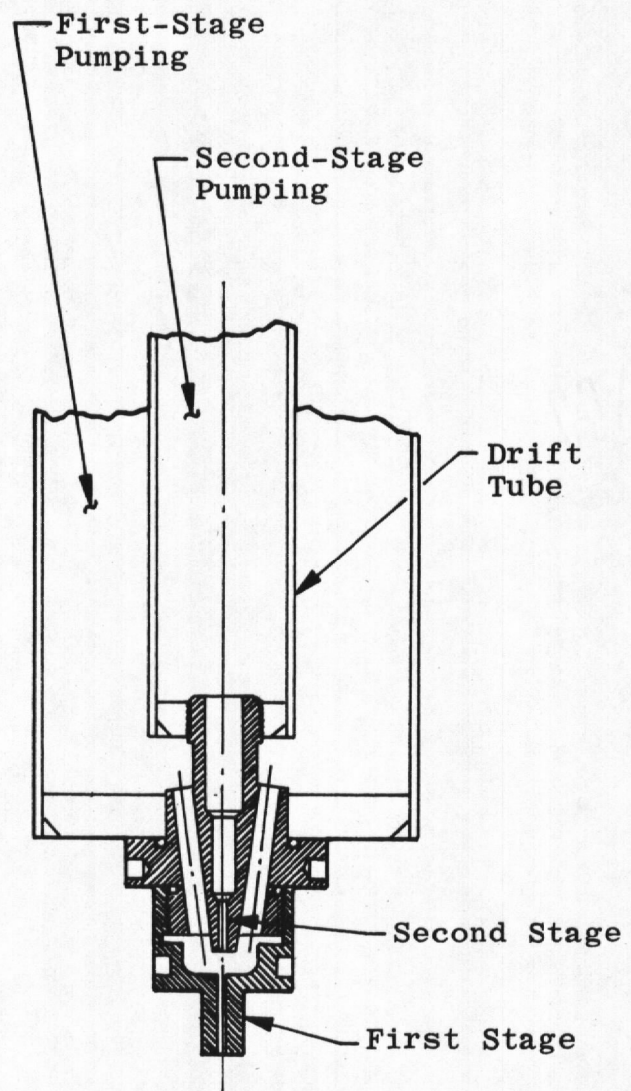


Fig. 7 Two-Stage Orifice

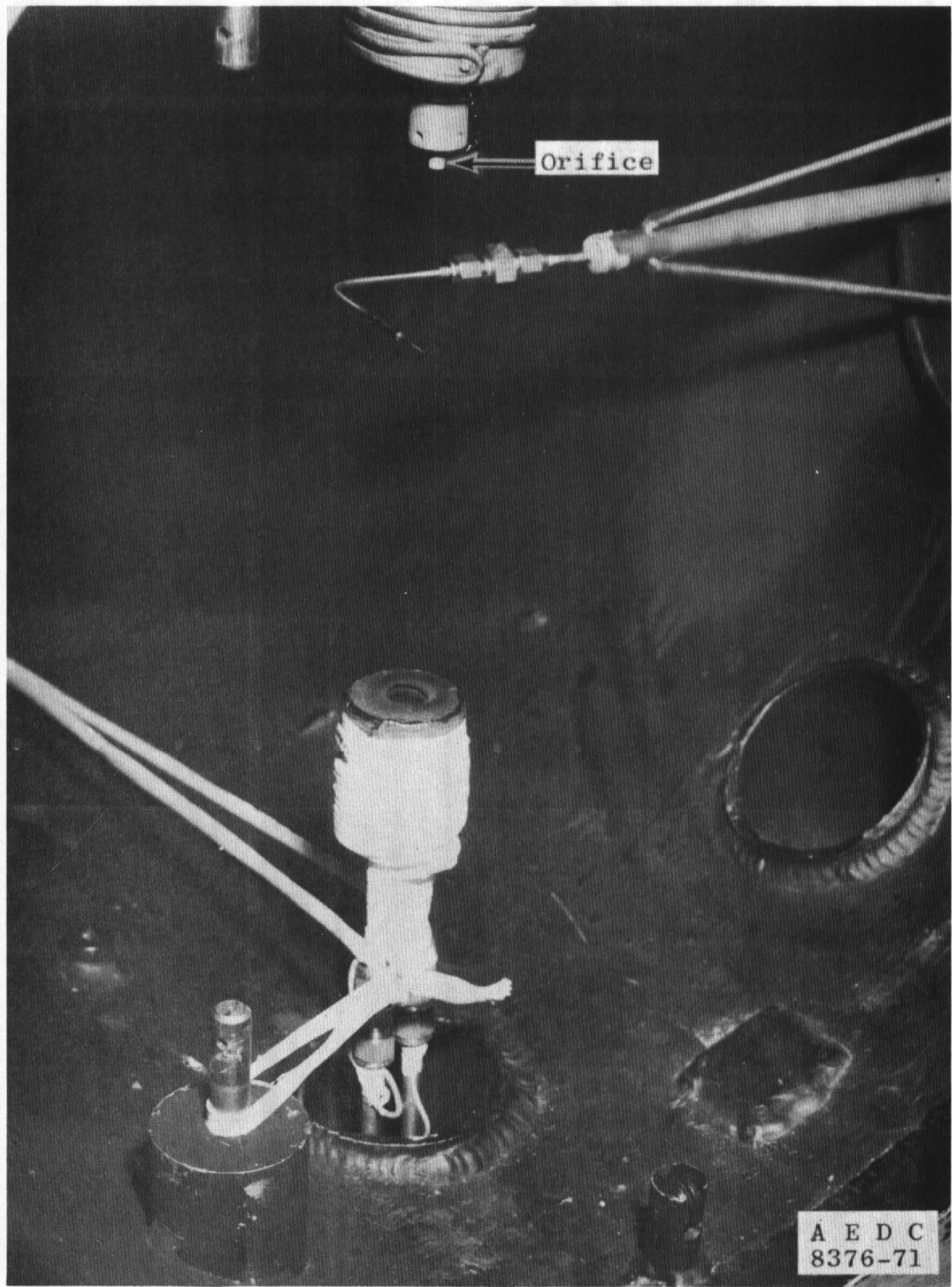


Fig. 8 Photograph of Drift Tube, Orifice, Collector Cup, and Pitot Probe in TCTR

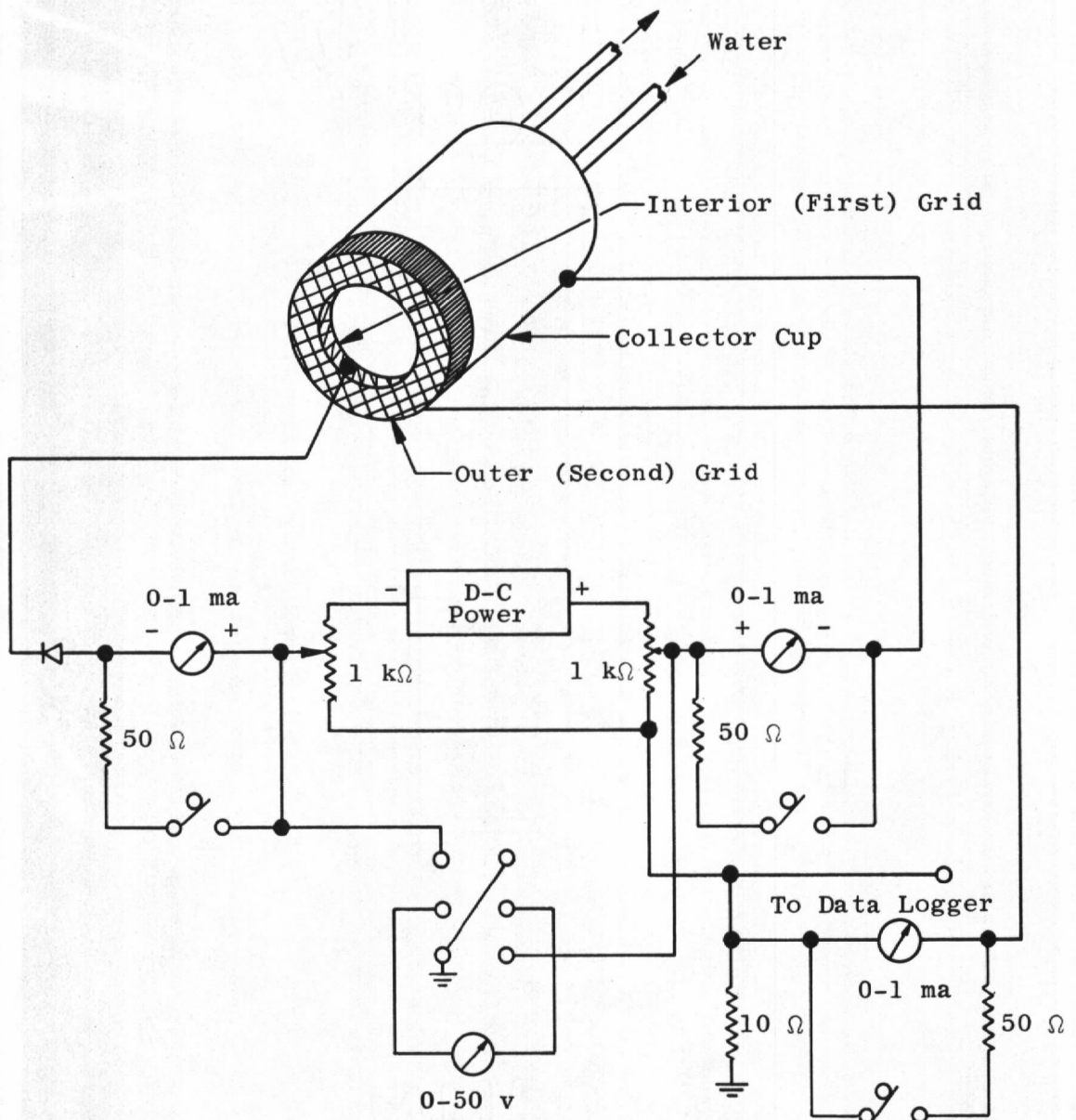


Fig. 9 Electron Beam Collector Cup

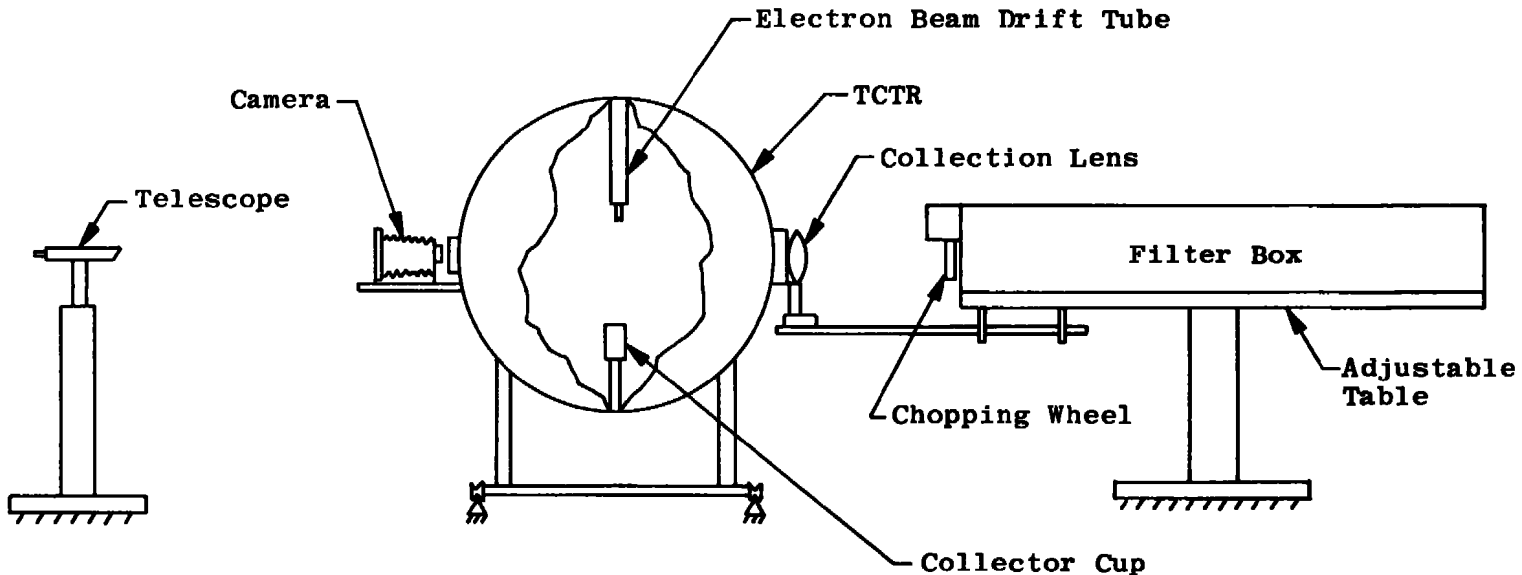


Fig. 10 Optical Equipment Arrangement around TCTR

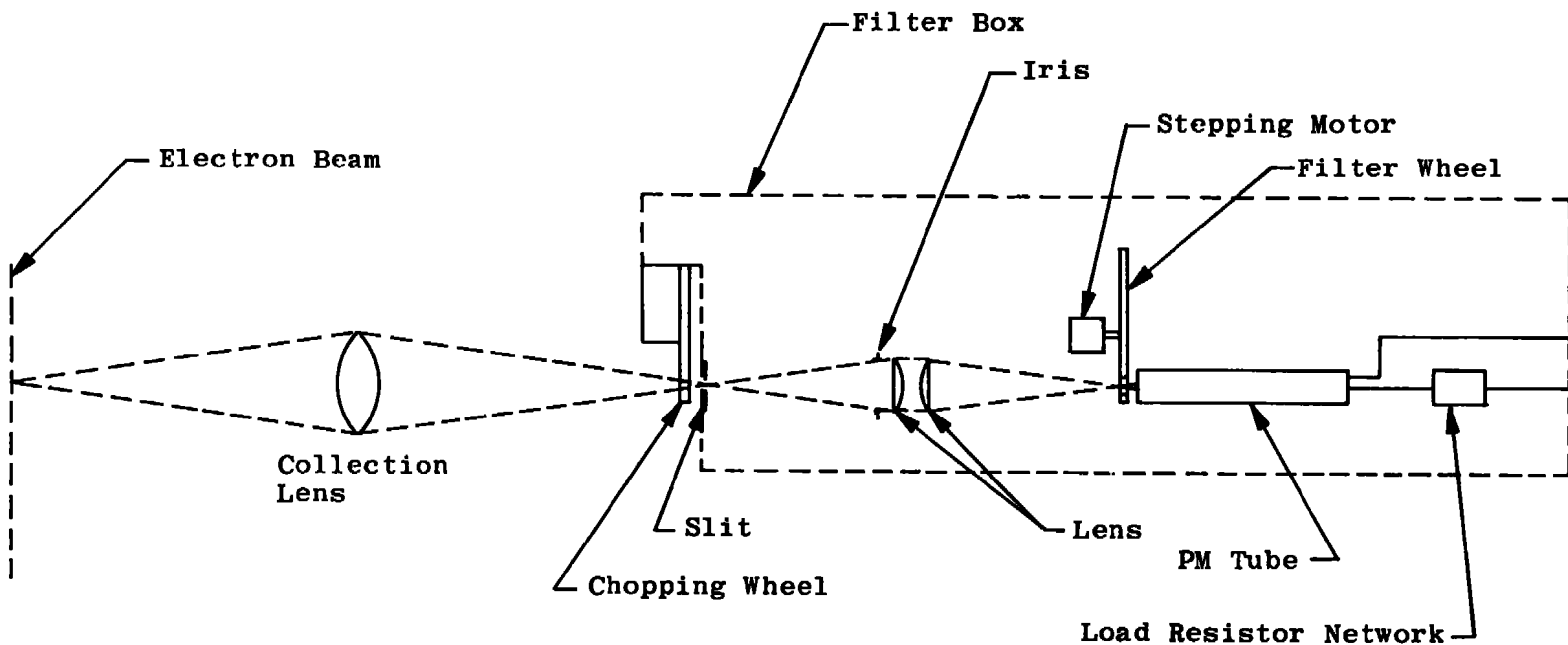


Fig. 11 Optical and Electronic System Schematic

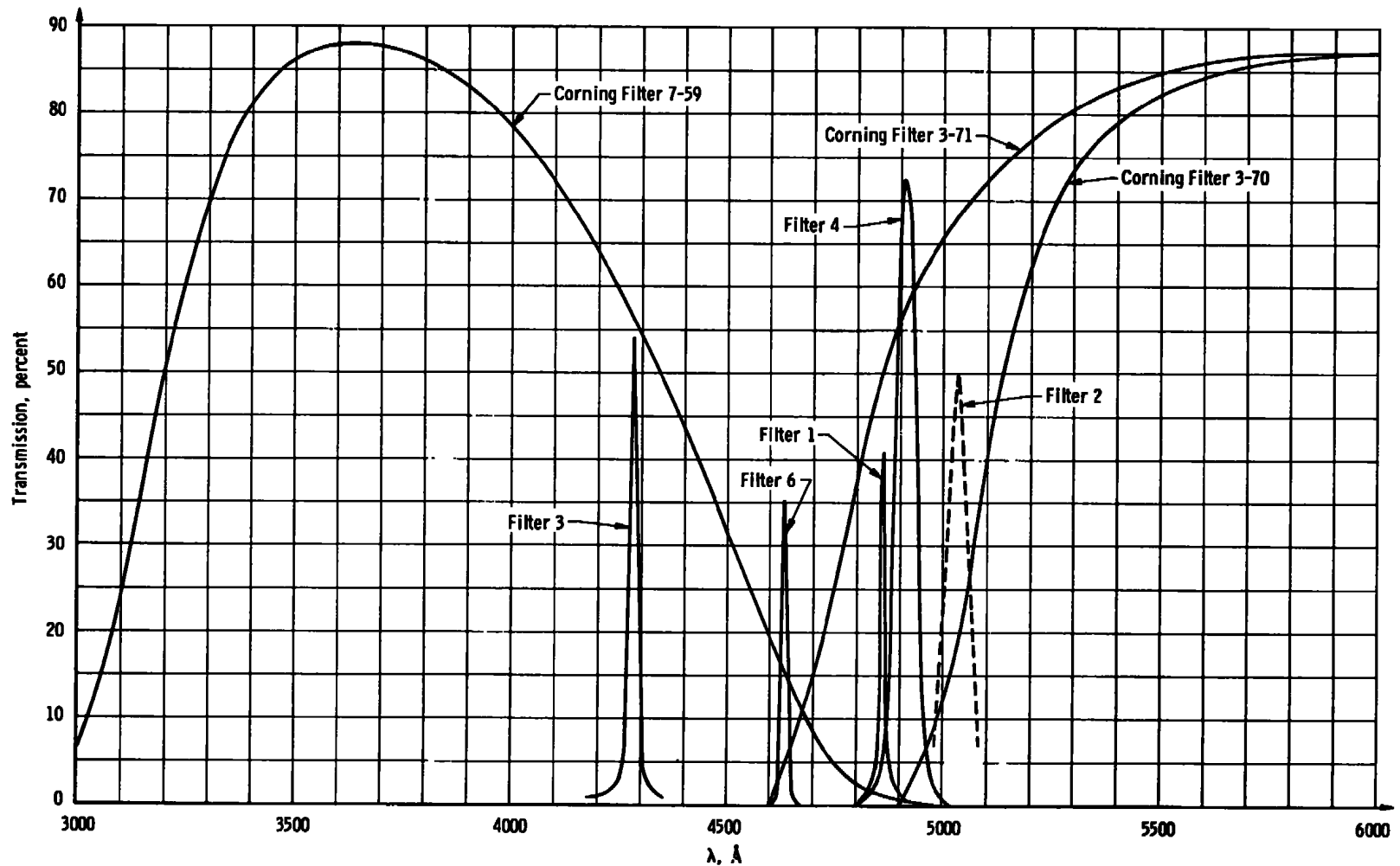


Fig. 12 Filter Transmission Curves

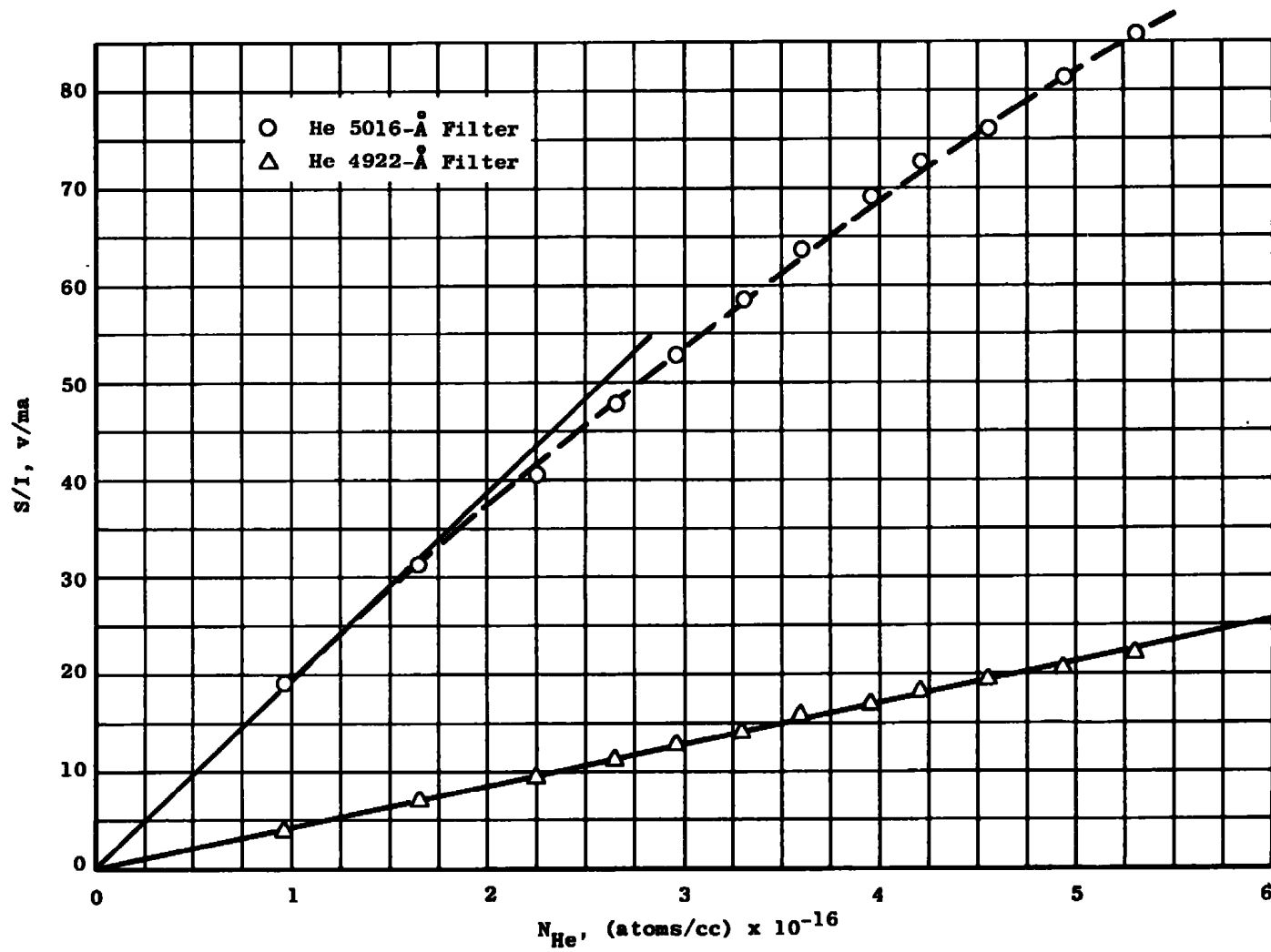


Fig. 13 Helium Signals as a Function of Helium Density

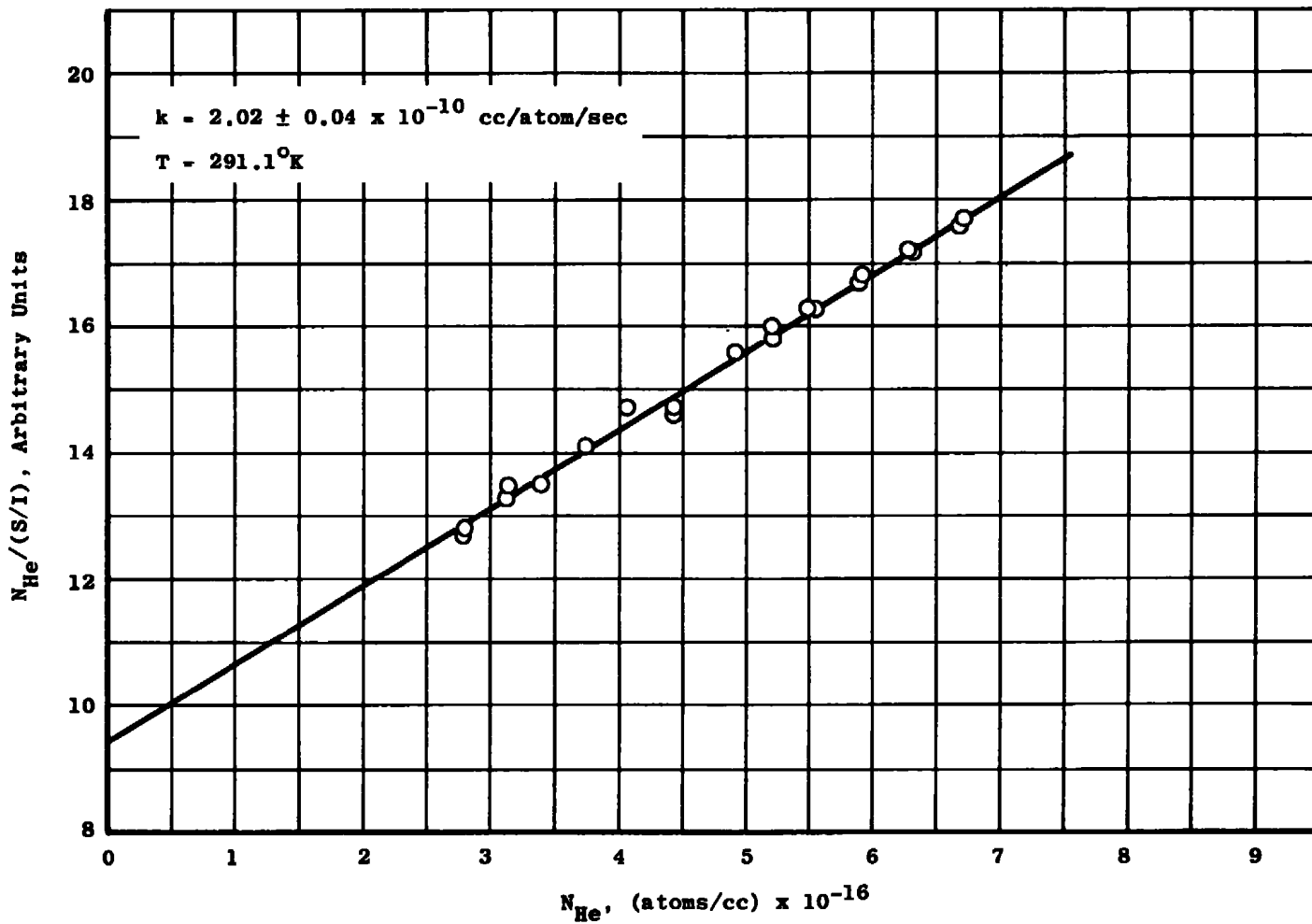


Fig. 14 Collisional Quenching Plot for He 3^1P , He 1^1S Collisions

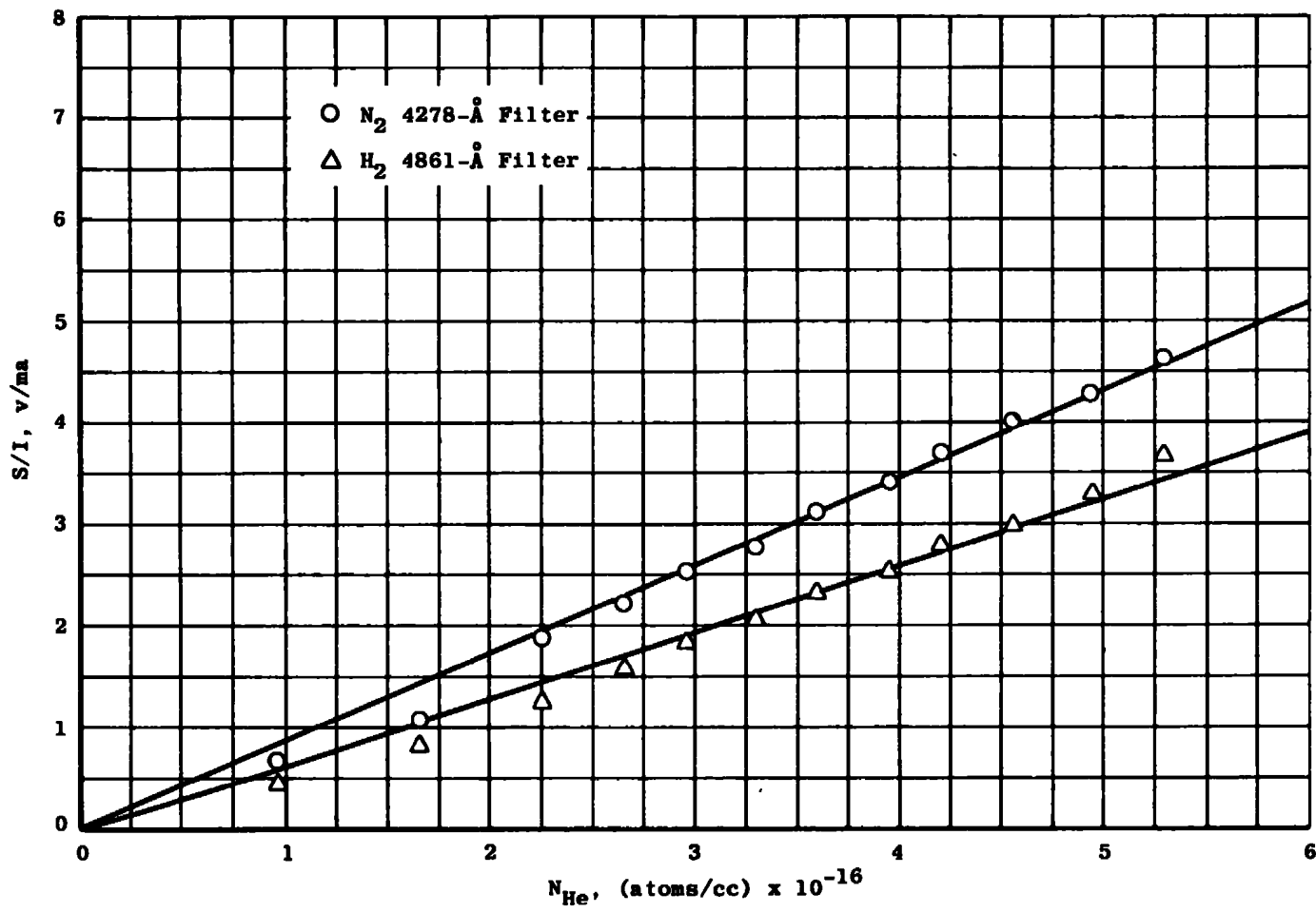


Fig. 15 Helium Cross-Talk Signal of Nitrogen and Hydrogen Filters

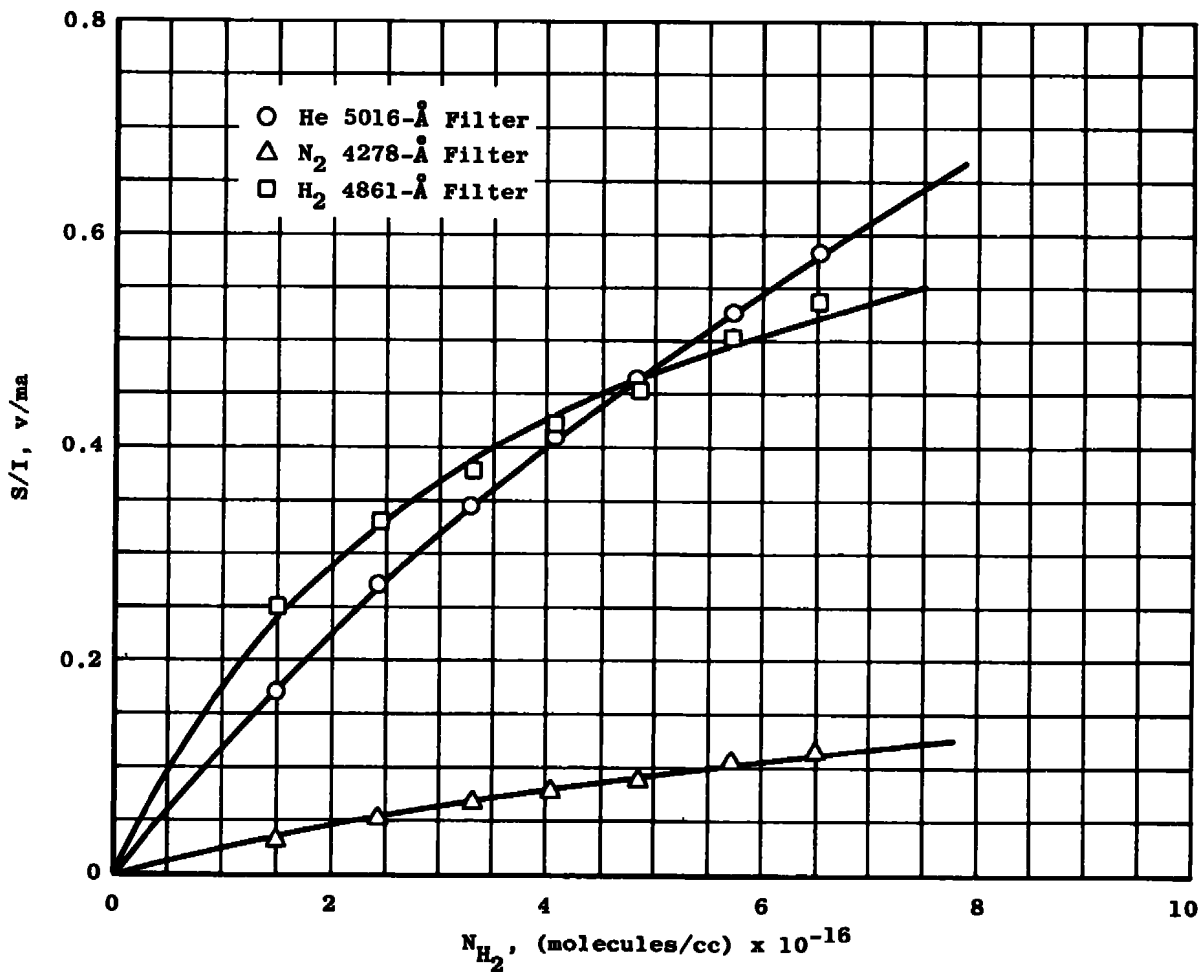


Fig. 16 Variation of Filter Signals with Hydrogen Density

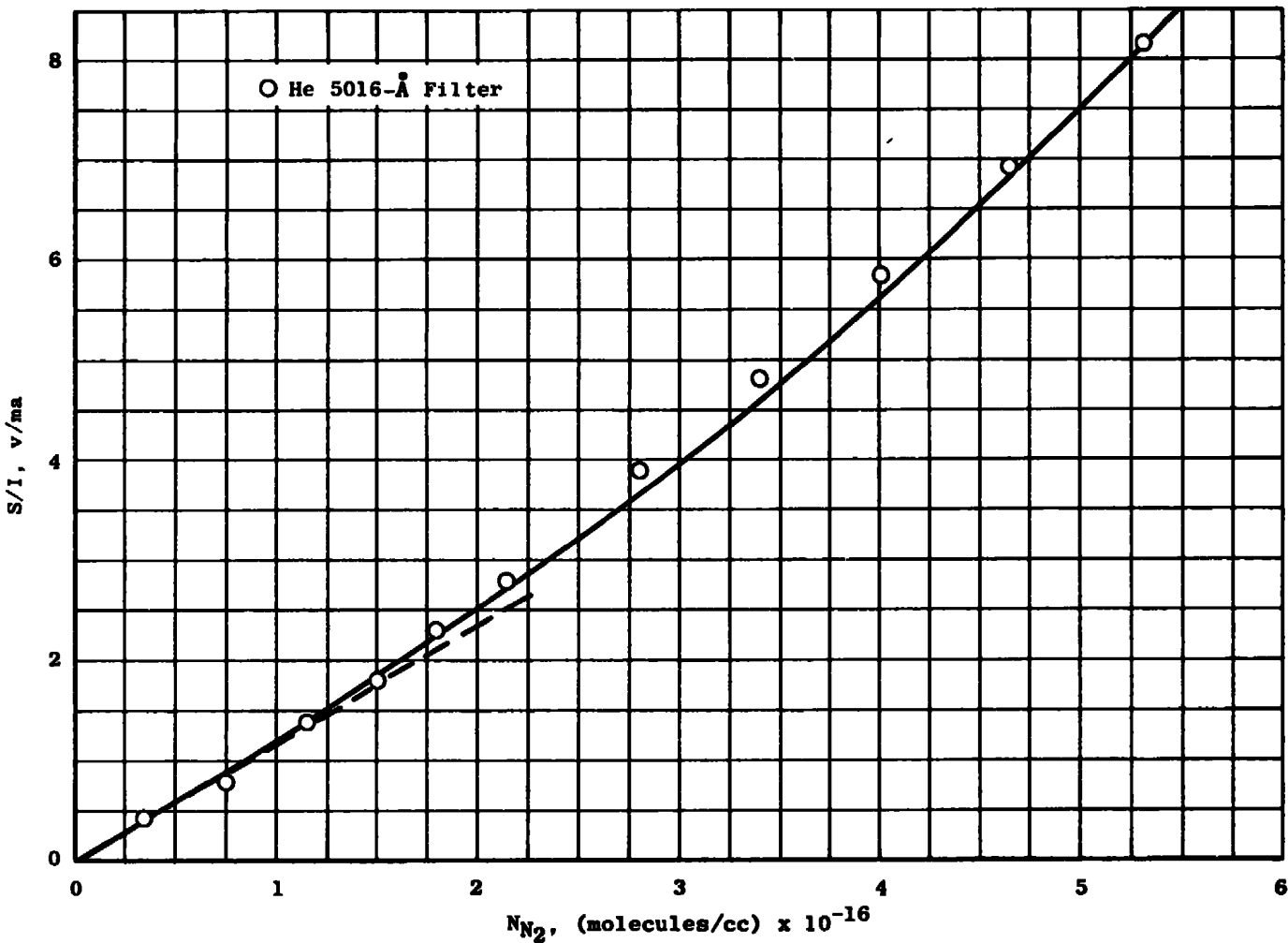


Fig. 17 Variation of Helium Filter Signal with Nitrogen Density

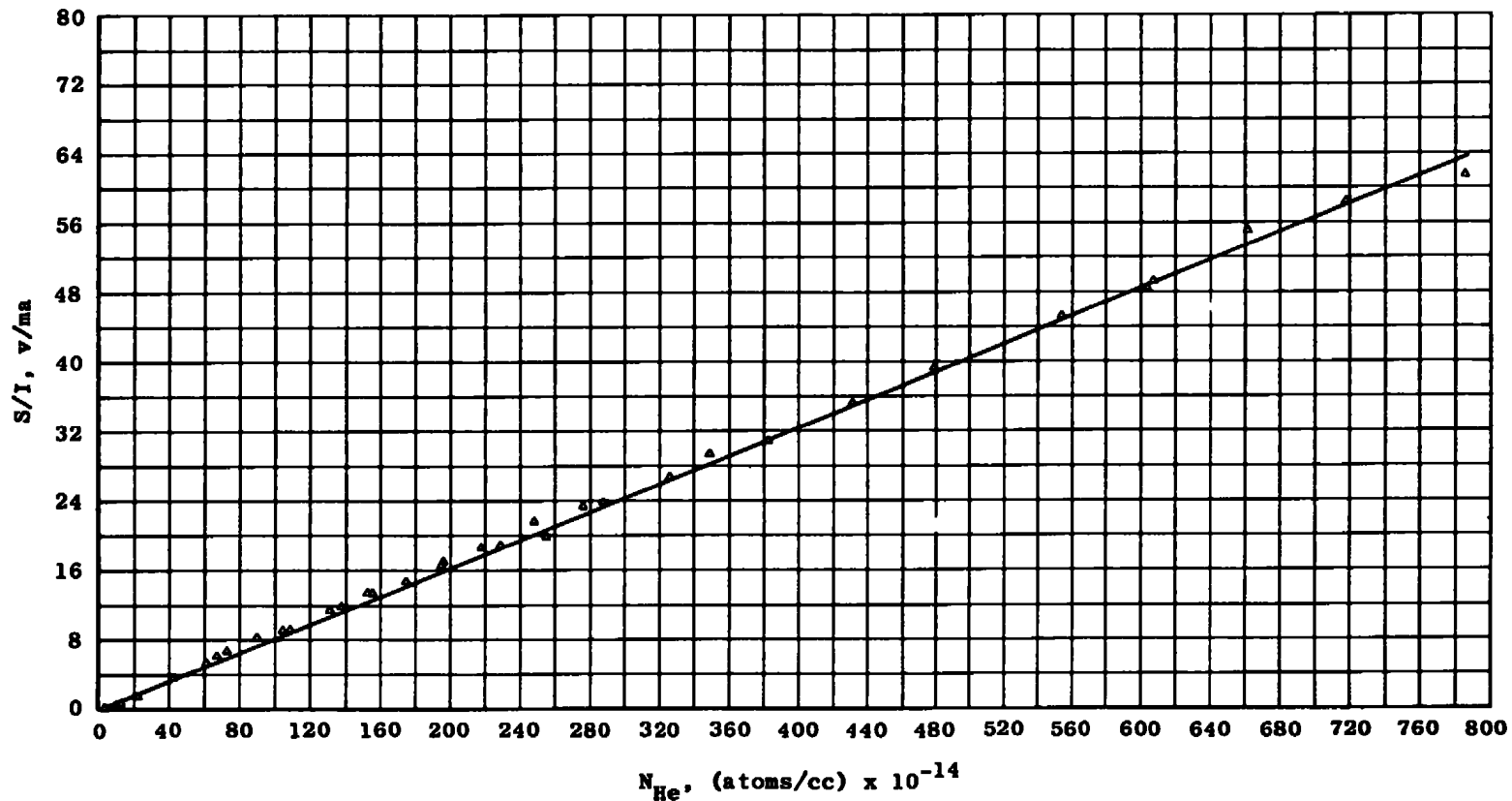


Fig. 18 In-Situ Helium Calibration

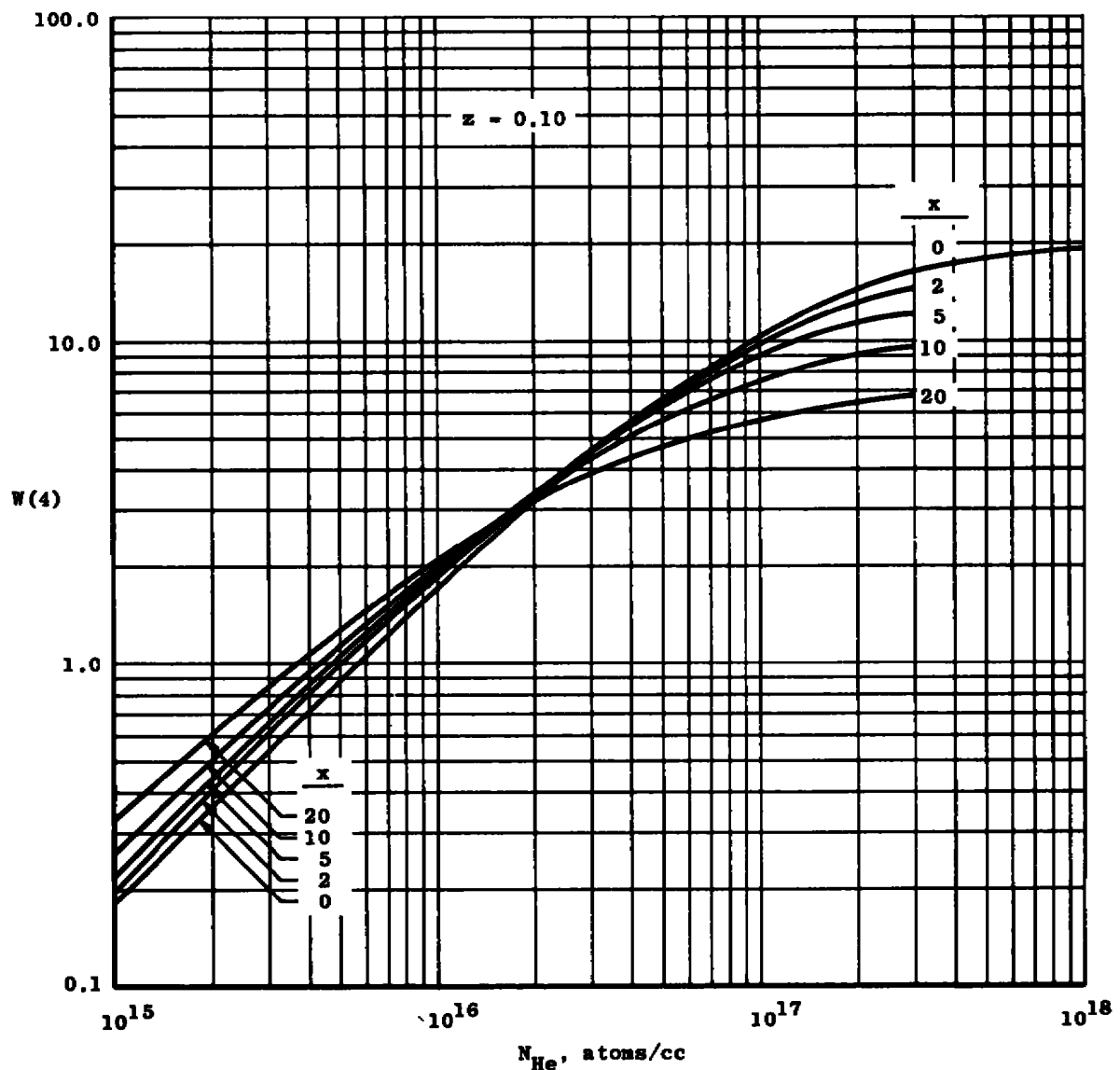


Fig. 19 Helium Filter Signal as a Function of Helium Density

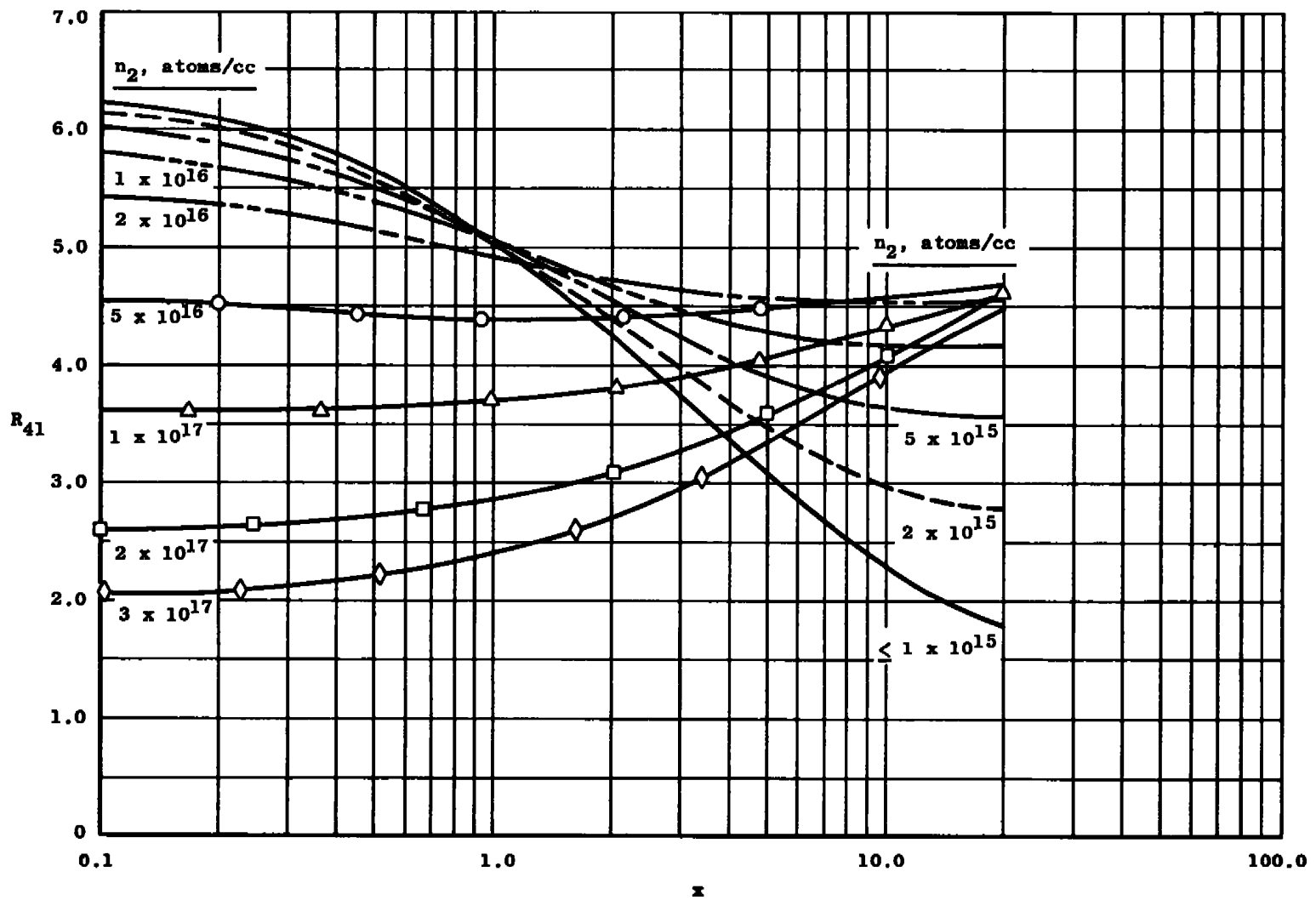


Fig. 20 Ratio of Helium and Hydrogen Filter Outputs versus x

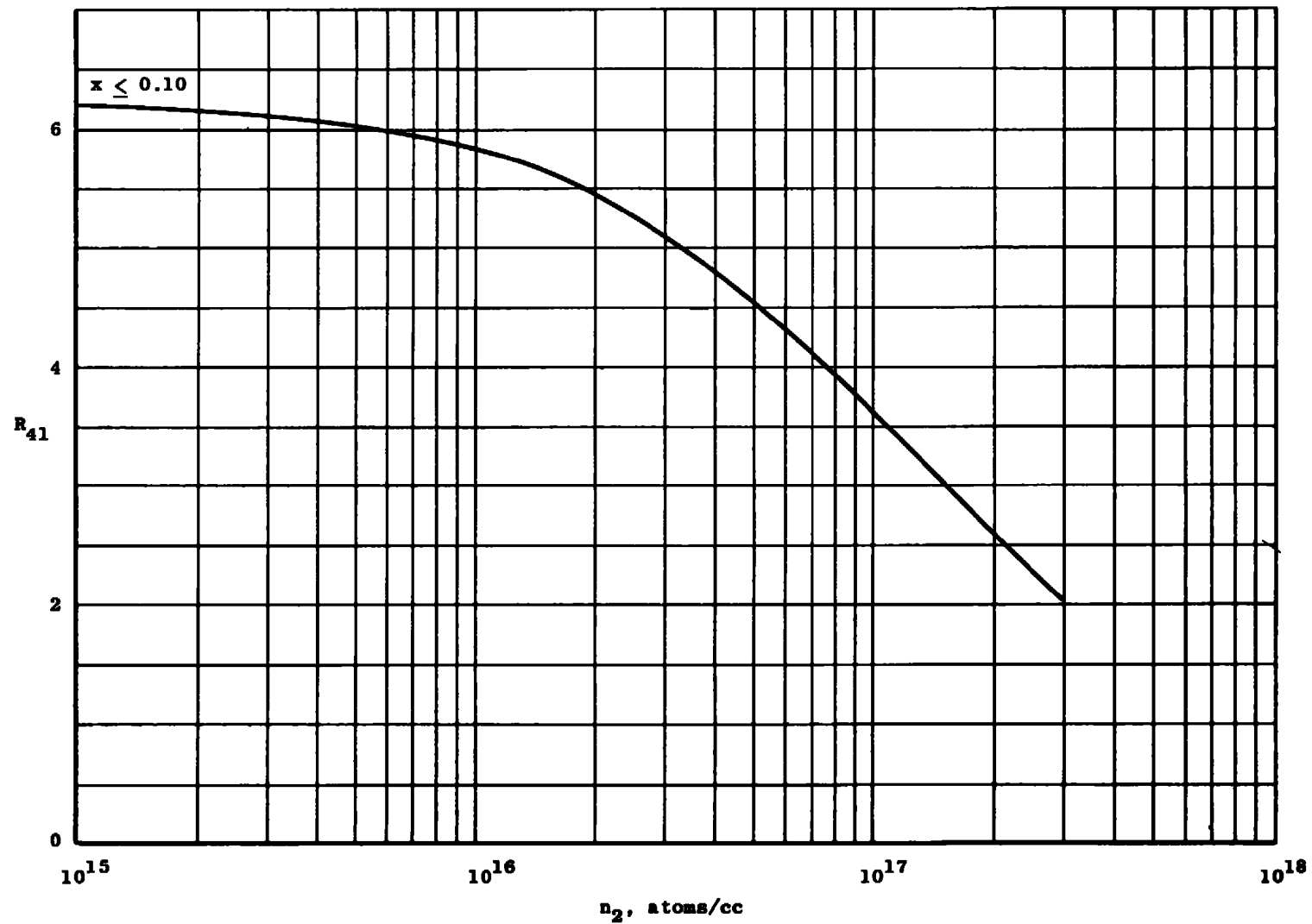


Fig. 21 Ratio of Helium and Hydrogen Filter Outputs versus Helium Density

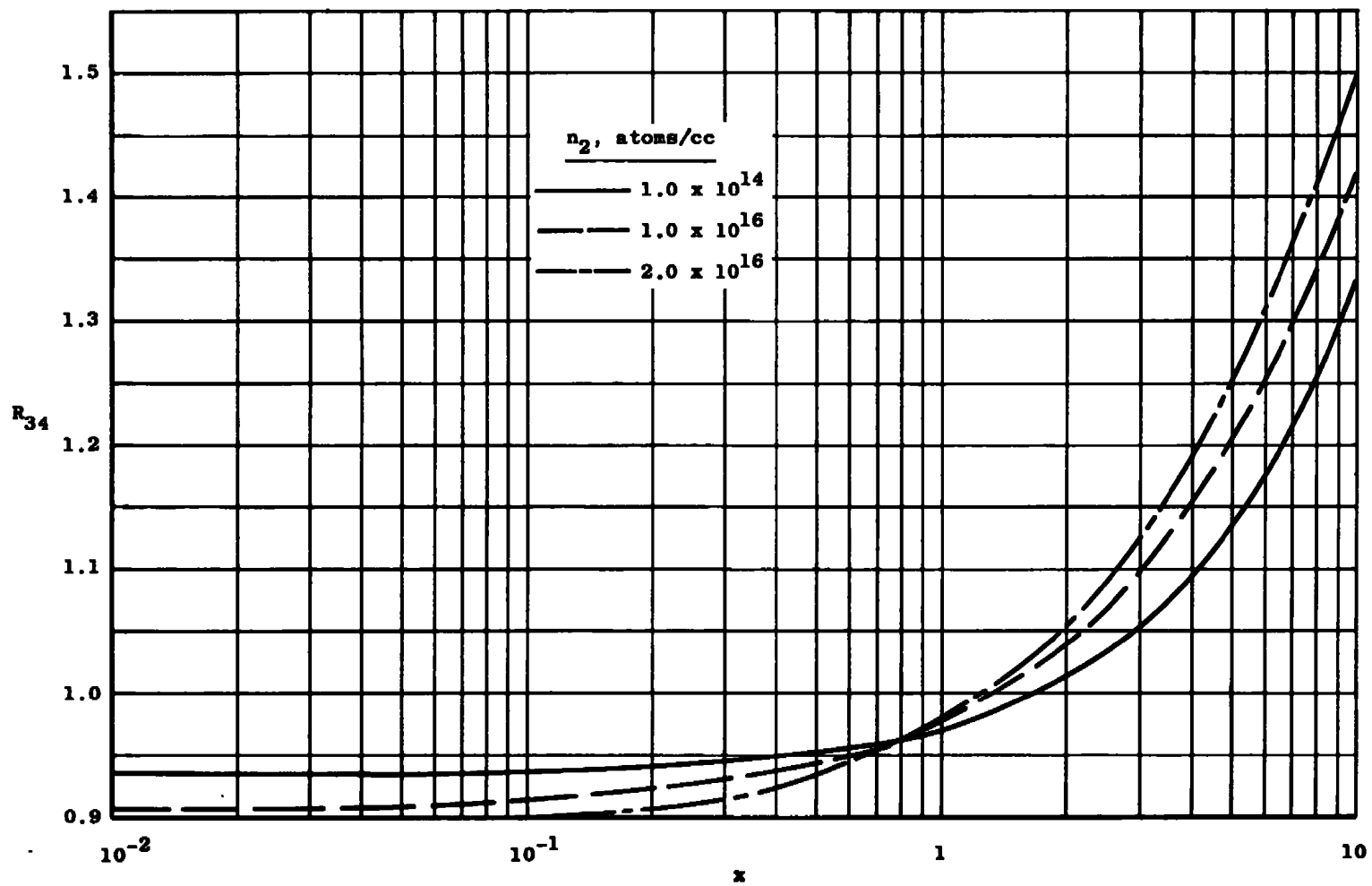


Fig. 22 Variation of R_{34} with x

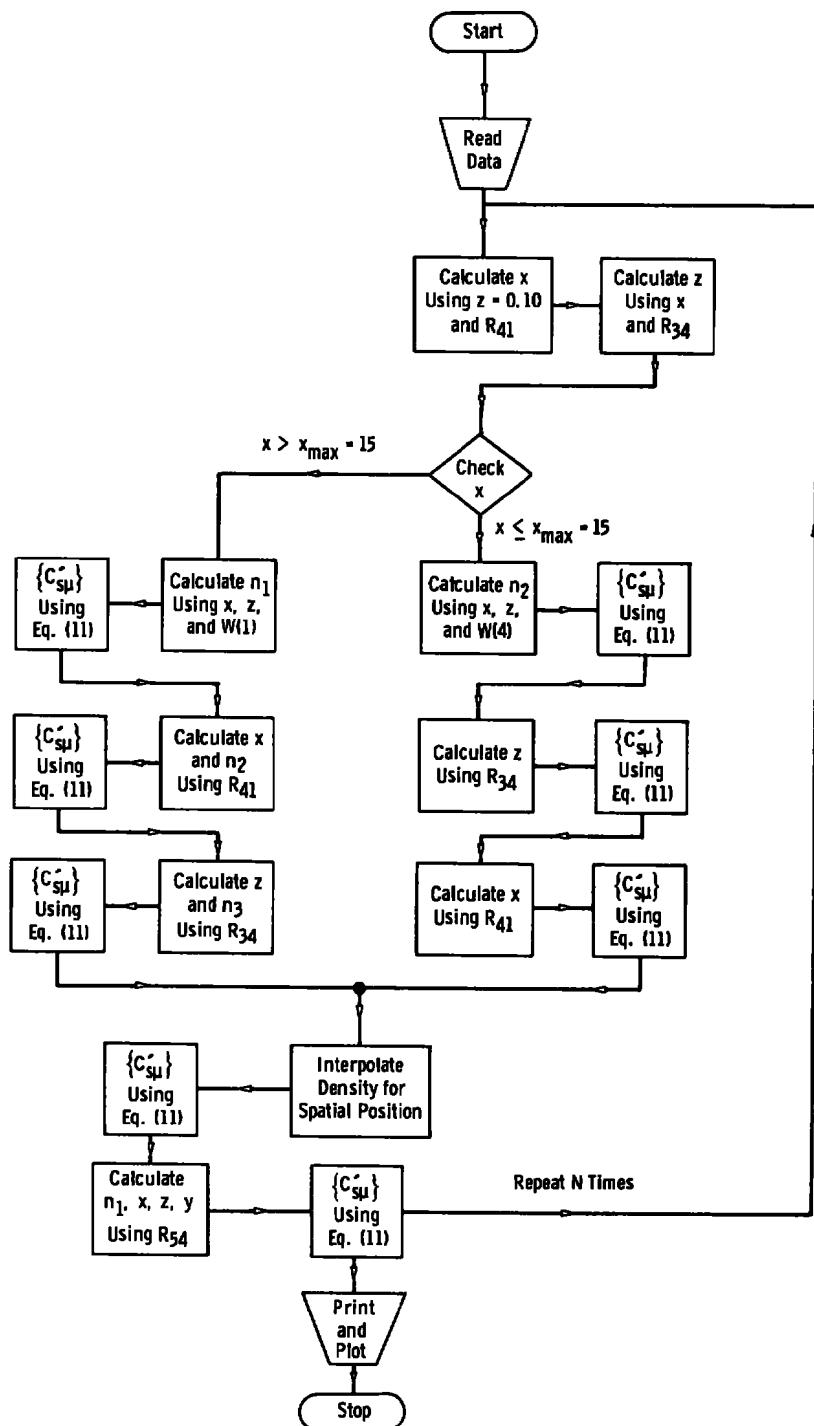


Fig. 23 Iteration Flow Chart

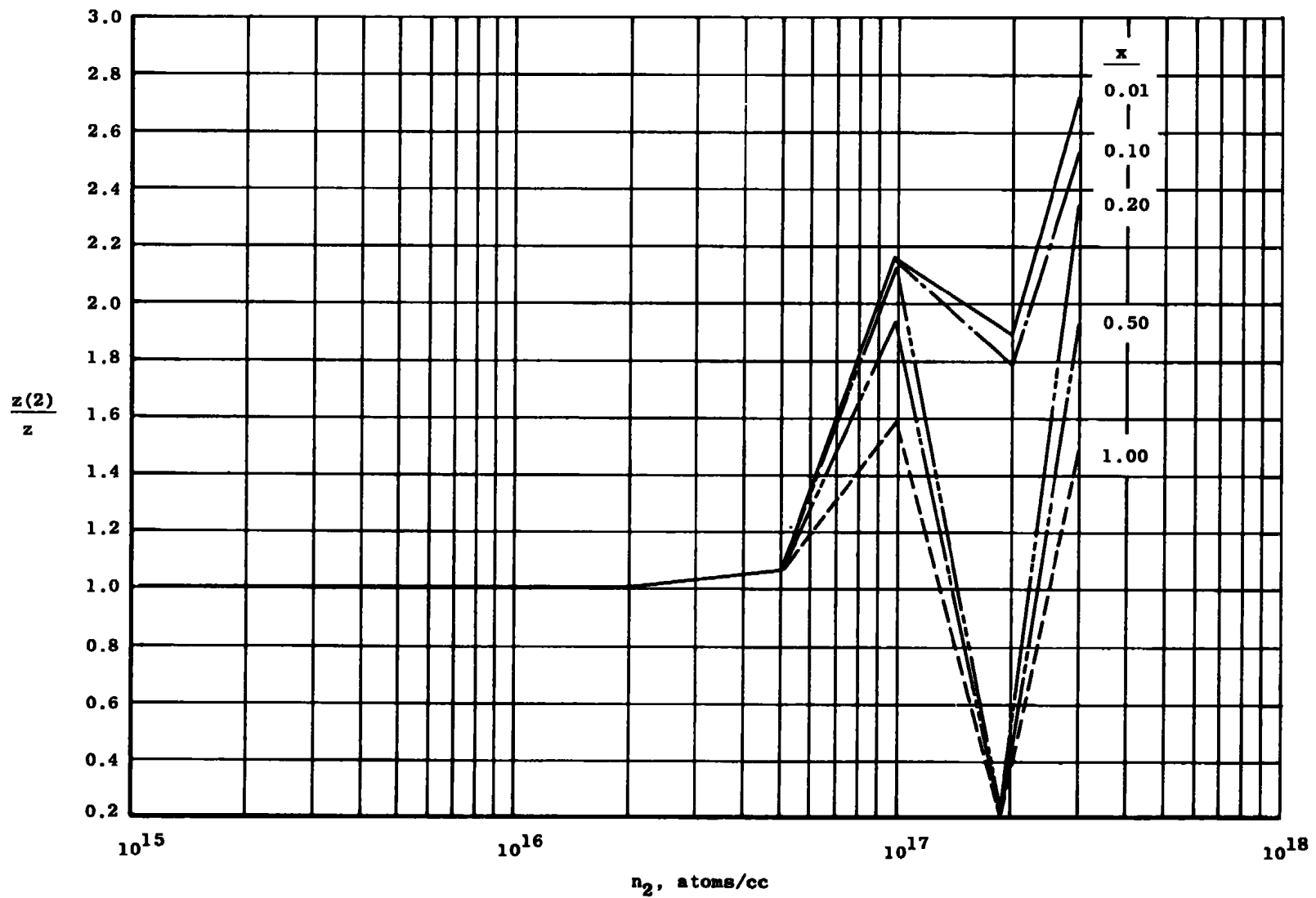


Fig. 24 Variation of Second Iteration of z with Helium Density

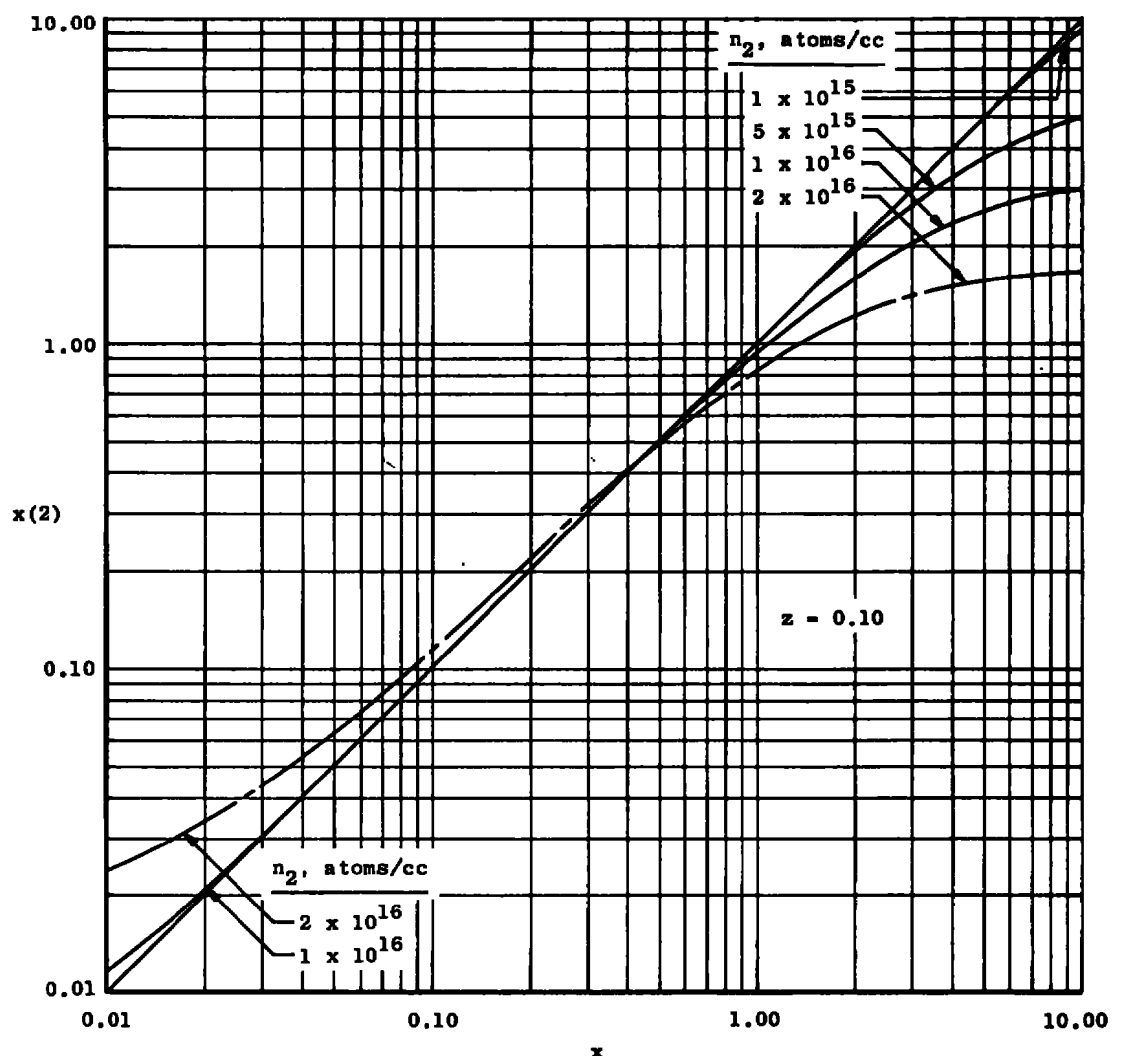


Fig. 25 Variation of Second Iteration of x with x

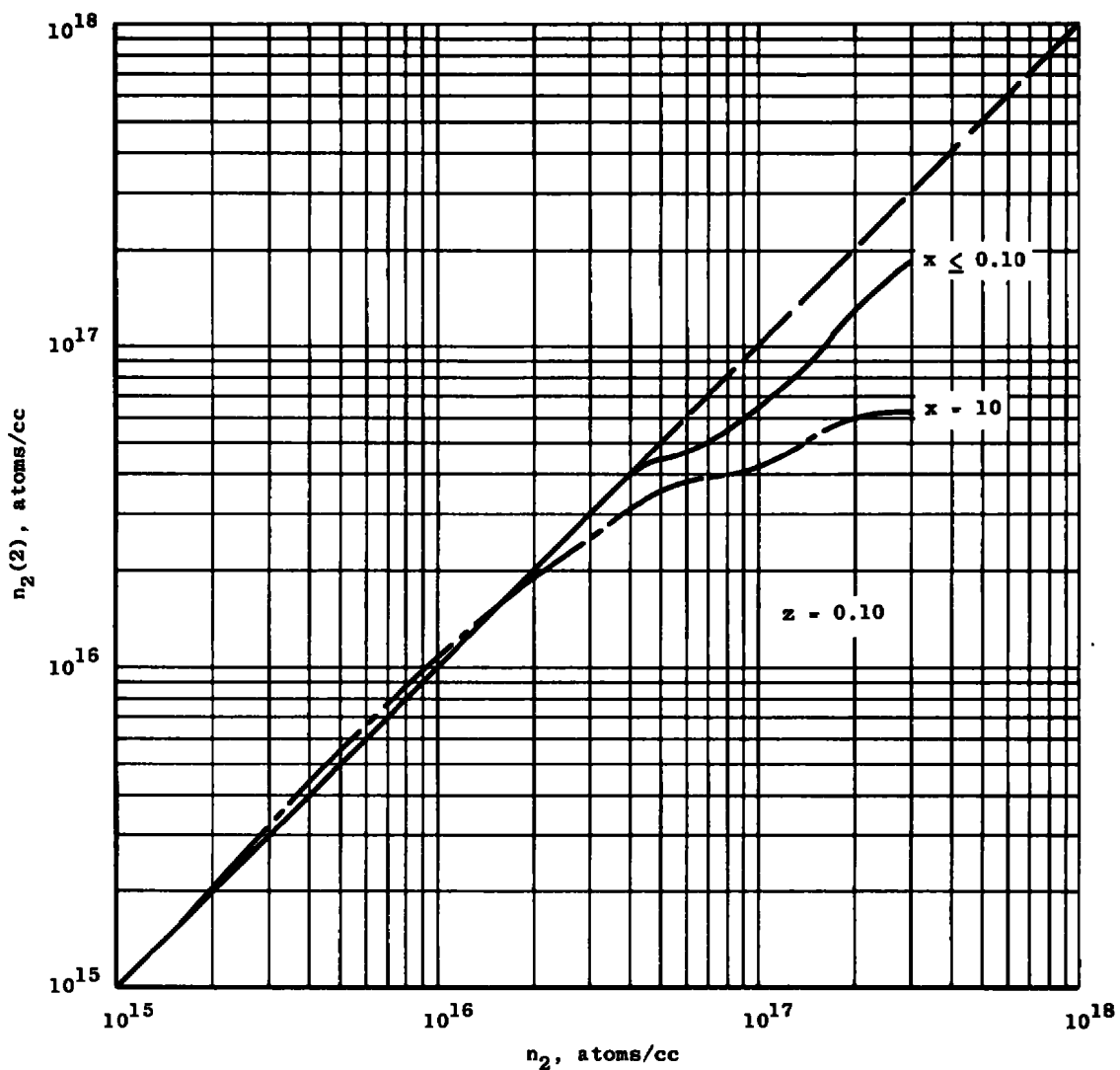


Fig. 26 Variation of Second Iteration of Helium Density with Helium Density

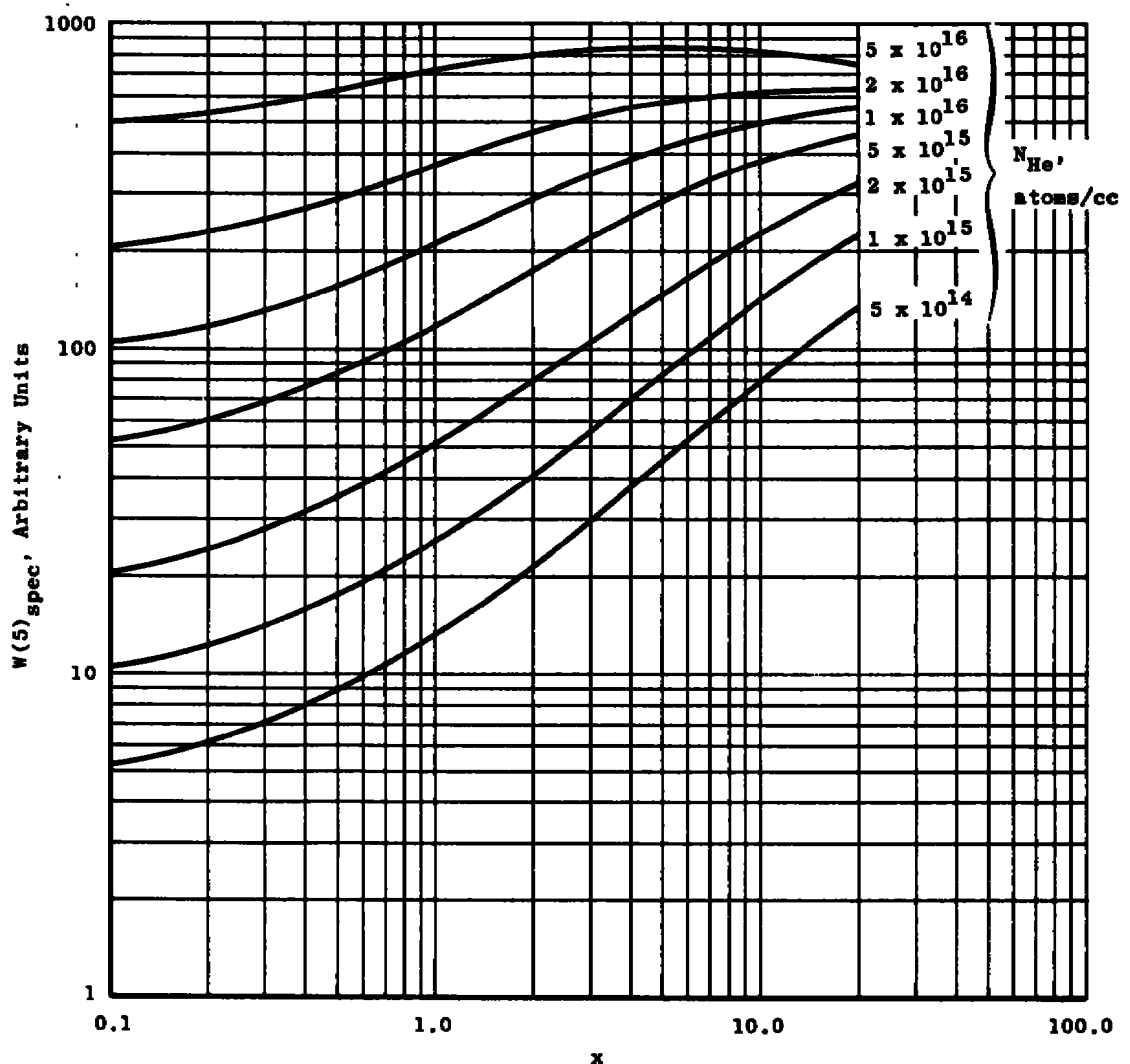


Fig. 27 Variation of Spectrometer Hydrogen Signal with Hydrogen Ratio x

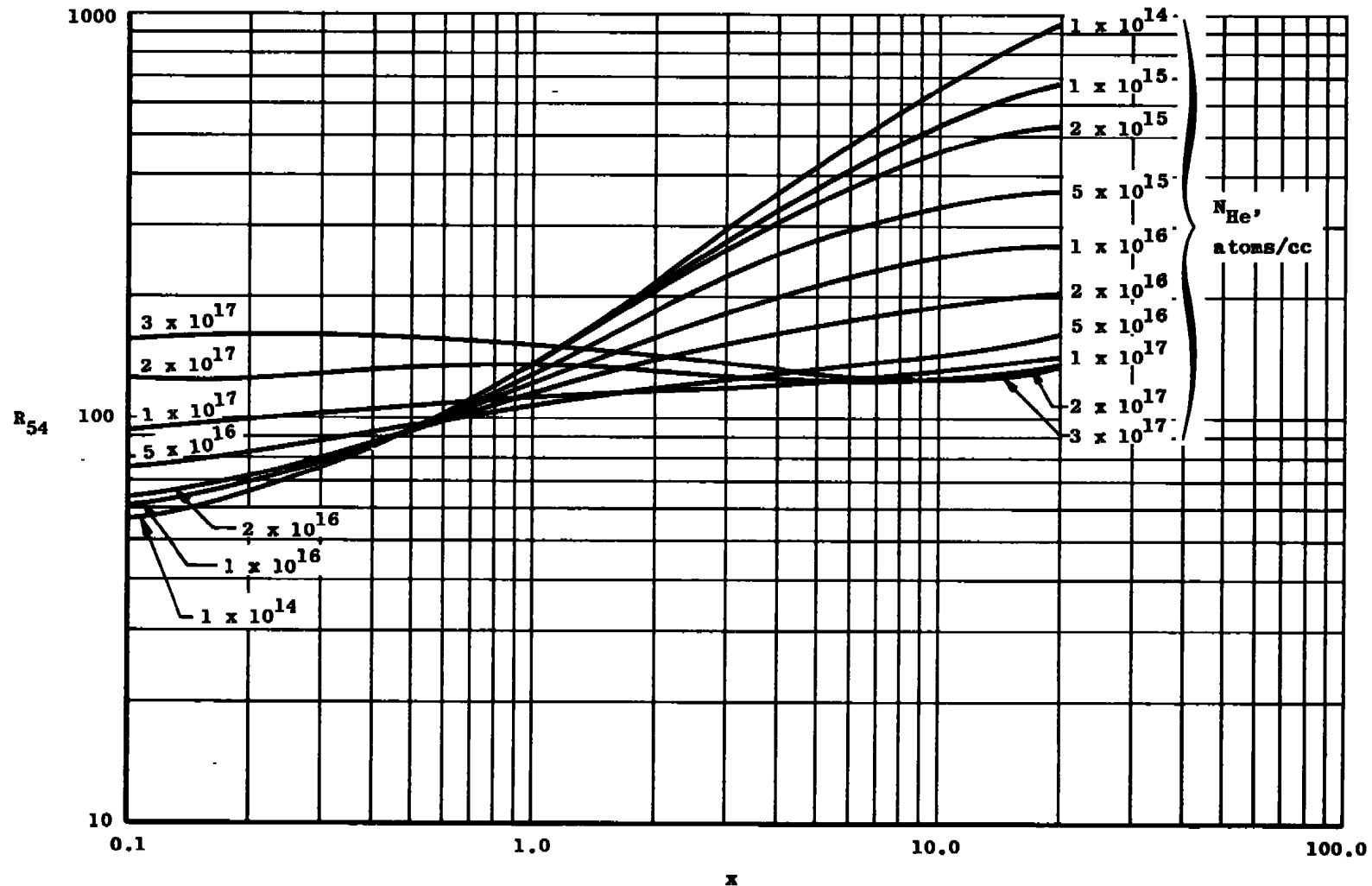


Fig. 28 Variation of Ratio R_{54} with Hydrogen Ratio x

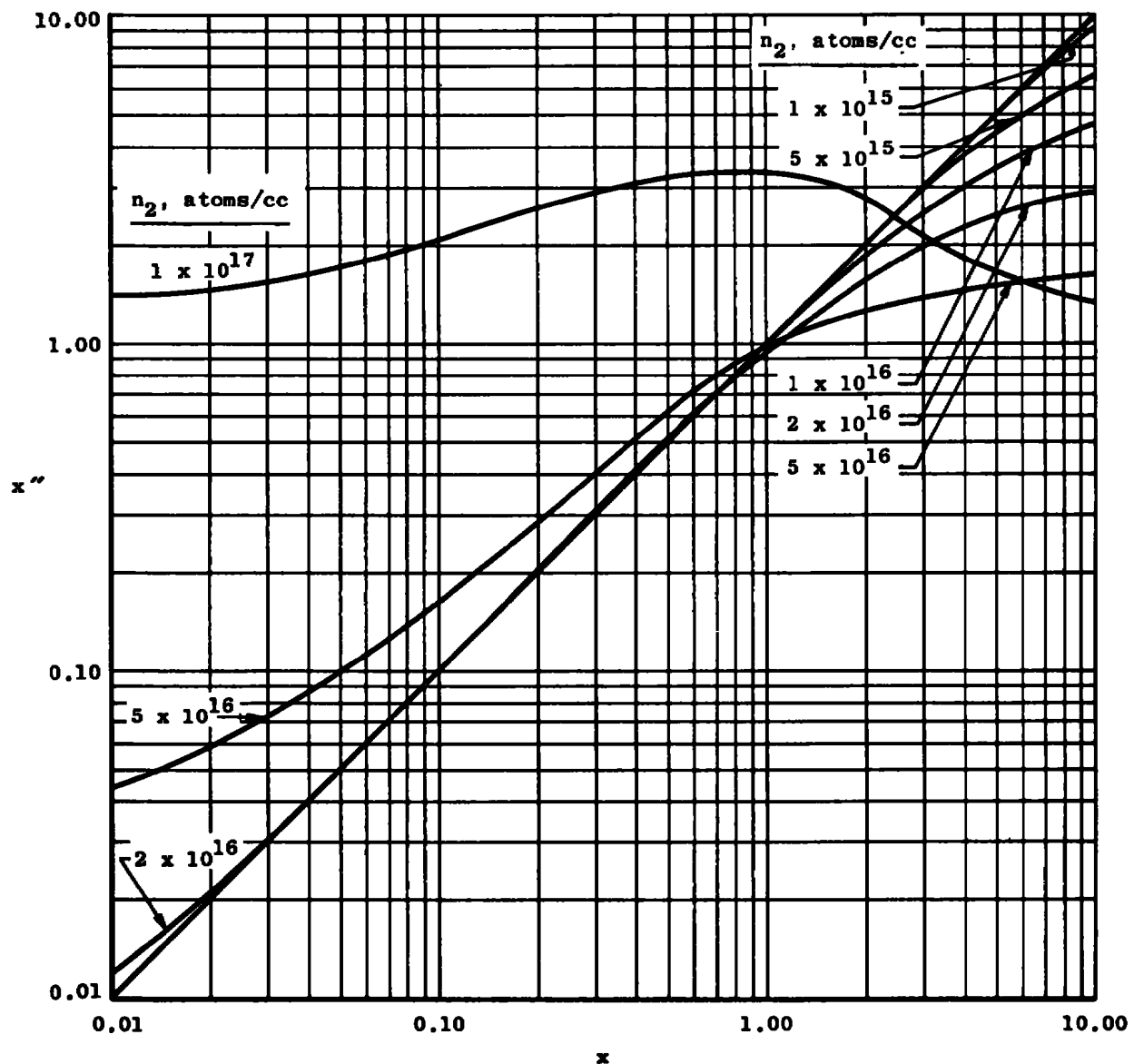


Fig. 29 Spectrometer Ratio x'' versus x

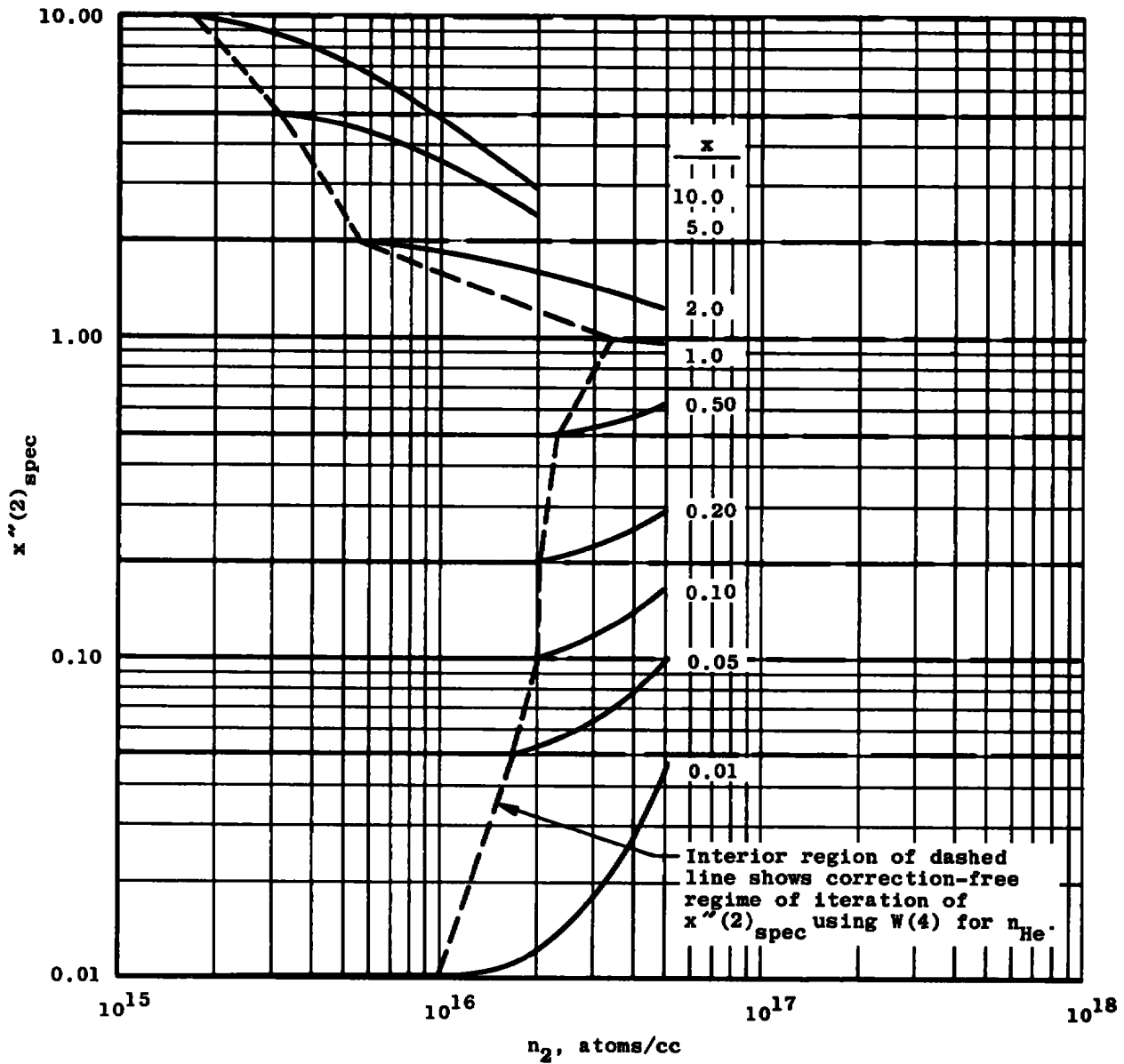


Fig. 30 Variation of Spectrometer Hydrogen Ratio with Helium Density

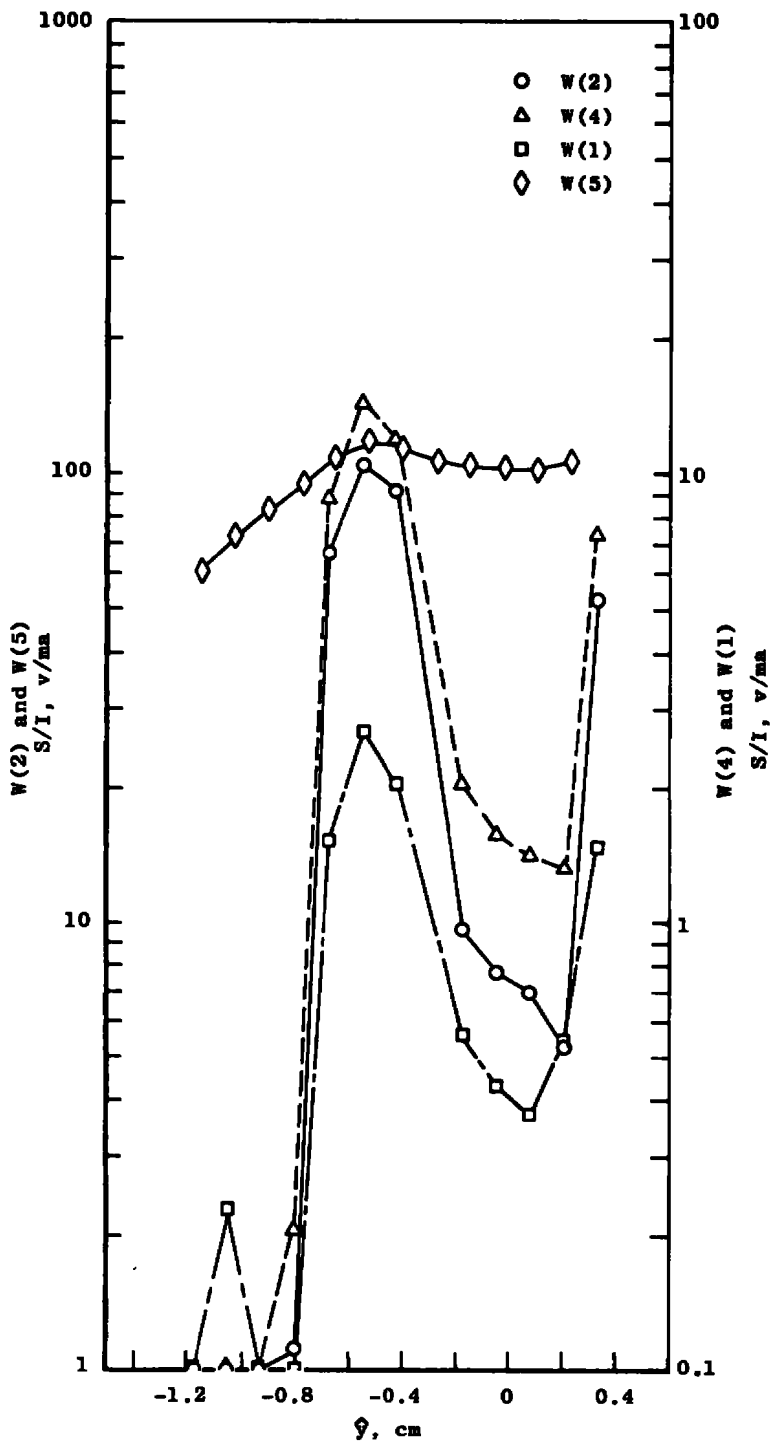


Fig. 31 Filter Signals at Profile 3, $x/d = 1.0$, Test Condition No. 6c

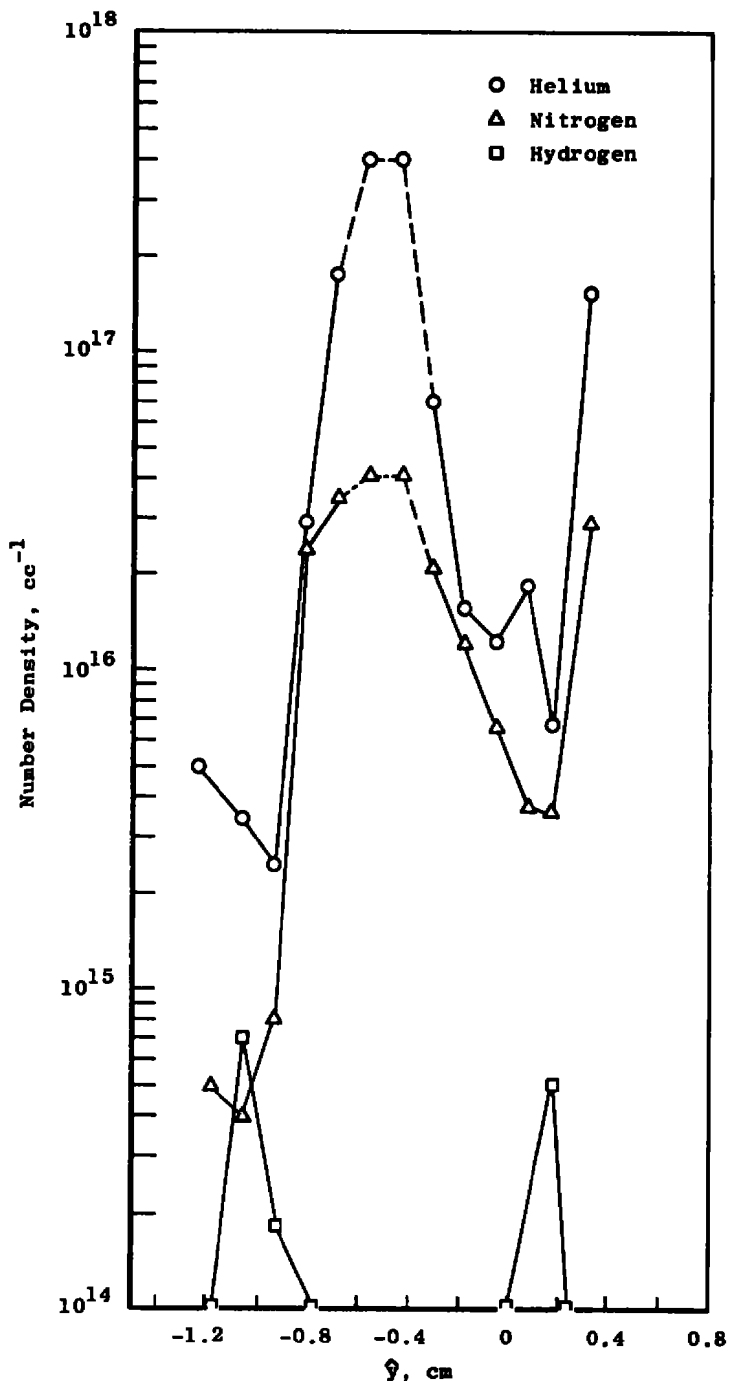


Fig. 32 Density Distribution for Profile 3, $\hat{x}/d = 0.13$, Test Condition No. 6c

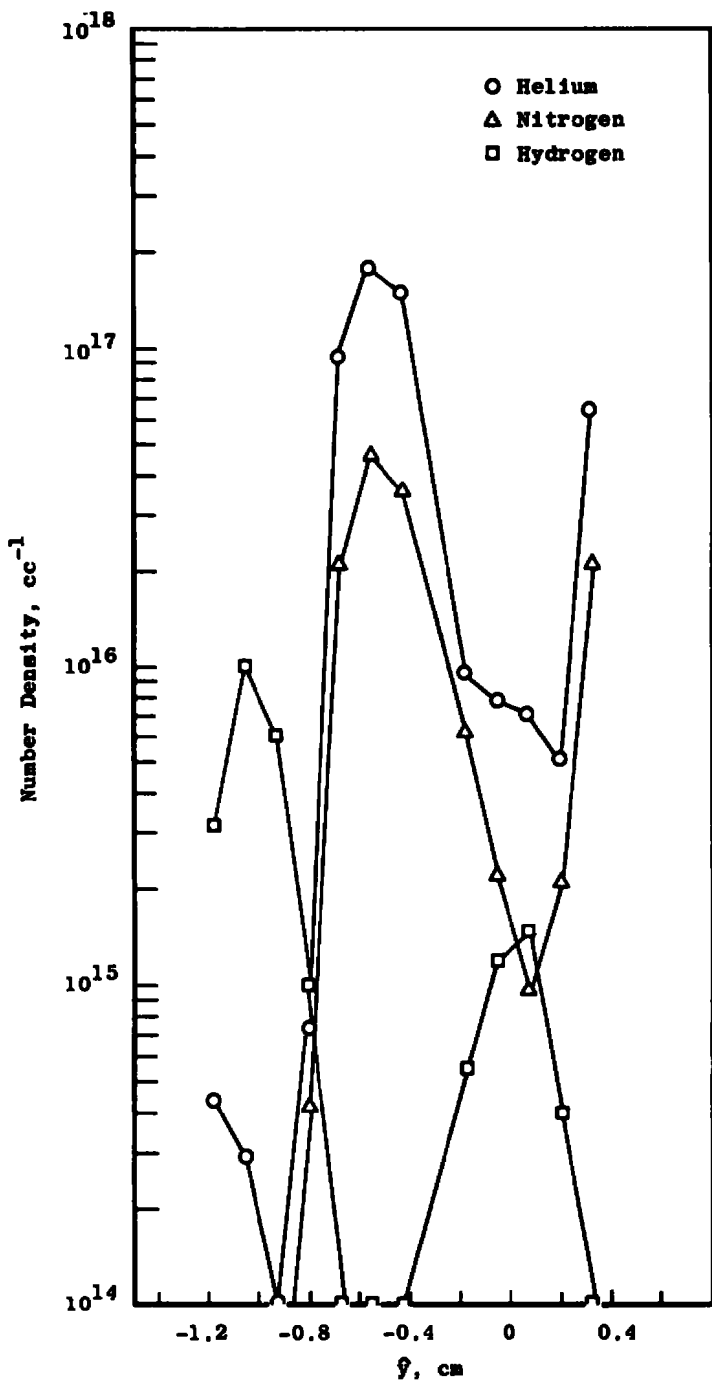


Fig. 33 Density Distribution for Profile 3, $\hat{x}/d = 1.0$, Test Condition No. 6c

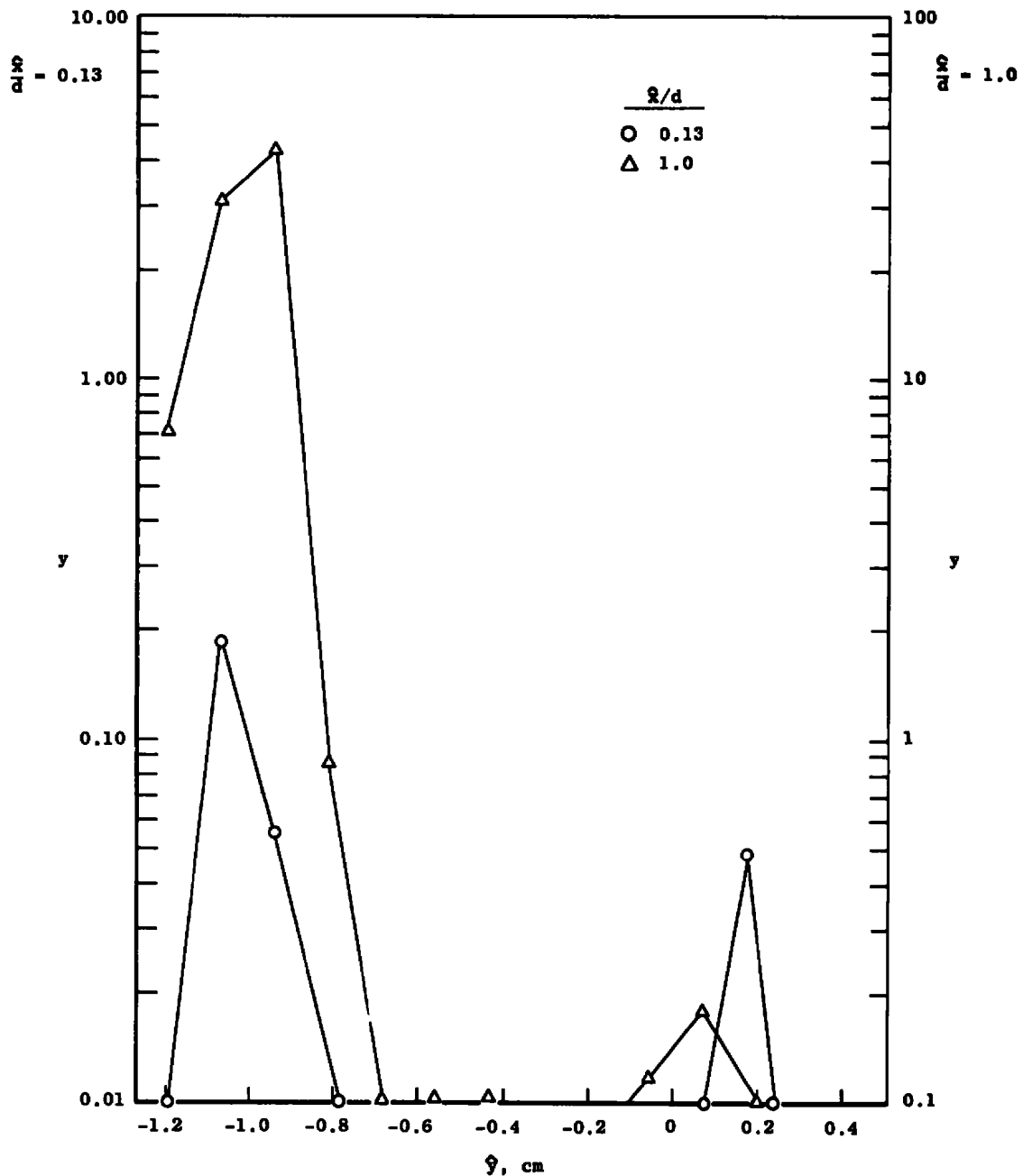


Fig. 34 Mixing-Ratio Distribution for Profile 3, $\hat{x}/d = 0.13$ and 1.0,
Test Condition No. 6c

TABLE I
RADIATIVE SYSTEMS AND FILTER SPECIFICATIONS

Species	Wavelength, Å	4278	4634	4861	4922	5016
H ₂			(1) H ₂ G → B (2) 25 Å	H _β 20 Å		
He					4 ¹ D → 2 ¹ P 85 Å	3 ¹ P → 2 ¹ S 100 Å
N ₂		N ₂ ⁺ (0, 1) 35 Å				

Legend: (1) Primary transition at indicated wavelength
 (2) Filter bandpass evaluated at 10-percent transmission points

TABLE II
EXCITATION COEFFICIENTS AND RATIOS

$s \backslash \mu$	1	2	3
1	(1) 1.17 (-2) (2) 9.50 (-18)	3.36 (-2) 2.72 (-17)	1.67 (-2) 1.35 (-17)
2	6.54 (-3) 5.29 (-18)	1.00 8.09 (-16)	6.08 (-2) 4.92 (-17)
3	1.23 (-3) 9.92 (-19)	4.47 (-2) 3.62 (-17)	1.99 1.61 (-15)
4	1.15 (-2) 9.30 (-18)	2.22 (-1) 1.80 (-16)	4.38 (-2) 3.54 (-17)
5	---	---	---
	1.78 (-14)*	8.74 (-15)*	0.0

(1) $C_{s\mu}/C_{22}$ (2) $C_{s\mu}$ (test)

* C_{51} and C_{52} expressed in units of counts/sec/
molecule/ μ a; all others, in counts/sec/
molecule/ma.

Entries are to be interpreted as 6.54(-3) ≡
 6.54×10^{-3} .

TABLE III
COLLISIONAL QUENCHING COEFFICIENTS

$s \backslash \mu$	1	2	3
1	(1) 3.20 (-17) (2) 5.0 (-18)** (3) 5.0 (-18)**	1.0 (-18) 0.00* 1.0 (-18)	1.0 (-18) 1.0 (-18) 1.42 (-18)
	6.3 (-18)* 1.0 (-18)** 1.0 (-18)**	5.0 (-18)** 1.65 (-17) 0.00*	1.0 (-18)** 1.0 (-18)** 0.00*
	5.2 (-18)* 1.0 (-18)** 1.0 (-18)**	1.0 (-18)** 0.00* 1.0 (-18)**	5.0 (-18)** 5.0 (-18)** 1.65 (-17)
4	1.0 (-17)* 1.0 (-18)** 1.0 (-18)**	1.0 (-18)** 8.0 (-18) 1.0 (-18)**	1.0 (-18)** 1.0 (-18)** 1.0 (-18)*
	3.20 (-17) 5.0 (-18)** 5.0 (-18)**	1.0 (-18)** 0.00* 1.0 (-18)**	1.0 (-18)** 1.0 (-18)** 1.42 (-18)*

Legend: (1) $\kappa_{\mu_1}^{(s)}$

(2) $\kappa_{\mu_2}^{(s)}$

(3) $\kappa_{\mu_3}^{(s)}$

e.g., $K_{11}^{(1)} = 3.20 (-17)$ is 3.20×10^{17}
cc/molecule

* Preliminary experimental measurements

** Estimated.

UNCLASSIFIED

Security Classification

DOCUMENT CONTROL DATA - R & D

(Security classification of title, body of abstract and indexing annotation must be entered when the overall report is classified)

1. ORIGINATING ACTIVITY (Corporate author) Arnold Engineering Development Center Arnold Air Force Station, Tennessee 37389		2a. REPORT SECURITY CLASSIFICATION UNCLASSIFIED
		2b. GROUP N/A
3. REPORT TITLE ELECTRON BEAM FLUORESCENCE DIAGNOSTICS OF A TERNARY GAS MIXTURE		
4. DESCRIPTIVE NOTES (Type of report and inclusive dates) Final Report -- September 15, 1971, to July 1, 1972		
5. AUTHOR(S) (First name, middle initial, last name) J. W. L. Lewis and W. D. Williams, ARO, Inc.		
6. REPORT DATE July 1973	7a. TOTAL NO. OF PAGES 74	7b. NO. OF REFS 6
8a. CONTRACT OR GRANT NO	9a. ORIGINATOR'S REPORT NUMBER(S) AEDC-TR-73-96	
b. PROJECT NO		
c. Program Element 62301F	9b. OTHER REPORT NO(S) (Any other numbers that may be assigned this report) ARO-VKF-TR-73-1	
10. DISTRIBUTION STATEMENT Approved for public release; distribution unlimited.		
11. SUPPLEMENTARY NOTES Available in DDC.	12. SPONSORING MILITARY ACTIVITY Air Force Rocket Propulsion Laboratory (RPCL), Edwards AFB, CA 93523	
13. ABSTRACT <p>The electron beam fluorescence technique was used for performing spatially resolved density measurements of a ternary gas mixture composed of helium, nitrogen, and hydrogen. The flow field studied was produced by a multinozzle array, and total gas density values exceeded 10^{17} molecules/cc within certain regions of the flow. The experimental apparatus, the procedures, and the method of data reduction used are discussed.</p> <p>2. Gases -- <i>Density</i> <i>Stagnation</i></p> <p>3 Density -- Measurement</p>		

UNCLASSIFIED

Security Classification

14. KEY WORDS	LINK A		LINK B		LINK C	
	ROLE	WT	ROLE	WT	ROLE	WT
electron beam						
exhaust plumes						
fluorescence						
density						
temperature						
helium						
nitrogen						
hydrogen						
collisional quenching						